ISSN 0869-5911, Petrology, 2016, Vol. 24, No. 4, pp. 409–432. © Pleiades Publishing, Ltd., 2016.
Original Russian Text © V.P. Sukhorukov, O.P. Polyansky, A.A. Krylov, S.V. Zinoviev, 2016, published in Petrologiya, 2016, Vol. 24, No. 4, pp. 441–464.

Reconstruction of the Metamorphic *P–T* Path from the Garnet Zoning in Aluminous Schists from the Tsogt Block, Mongolian Altai

V. P. Sukhorukov[a, b], O. P. Polyansky[a], A. A. Krylov[a], and S. V. Zinoviev[a]

[a] *Sobolev Institute of Geology and Mineralogy, Siberian Branch, Russian Academy of Sciences, pr. Akademika Koptyuga 3, Novosibirsk, 630090 Russia*

e-mail: svp@igm.nsc.ru

[b] *Novosibirsk State University, ul. Pirogova 2, Novosibirsk, 630090 Russia*

Received September 29, 2015; in final form, December 14, 2015

Abstract—The paper presents original authors' data on aluminous schists in the Tsogt tectonic plate in the Southern Altai Metamorphic Belt. The nappe includes a medium-temperature/medium-pressure zonal metamorphic complex, whose metamorphic grade varies from the greenschist to epidote-amphibolite facies. The garnet and garnet–staurolite schists contain three garnet generations of different composition and morphology. The *P–T* metamorphic parameters estimated by mineralogical geothermometers and geobarometers and by numerical modeling with the PERPLEX 668 software provide evidence of two successive metamorphic episodes: high-gradient (of the andalusite–sillimanite type, geothermal gradient approximately 40–50°/km) and low-gradient (kyanite–sillimanite type, geothermal gradient approximately 27°/km). The *P–T* parameters of the older episode are $T = 545–575$°C and $P = 3.1–3.7$ kbar. Metamorphism during the younger episode was zonal, and its peak parameters were $T = 560–565$°C, $P = 6.4–7.2$ kbar for the garnet zone and $T = 585–615$°C, $P = 7.1–7.8$ kbar for the staurolite zone. The metamorphism evolved according to a clockwise *P–T* path: the pressure increased during the first episode at a practically constant temperature, and then during the second episode, the temperature increased at a nearly constant pressure. Such trends are typical of metamorphism related to collisional tectonic settings and may be explained by crustal thickening due to overthrusting. The regional crustal thickening reached at least 15–18 km.

DOI: 10.1134/S0869591116040068

INTRODUCTION

Estimating physicochemical parameters of metamorphic processes is one of the key petrological problems. Understanding the circumstances, mechanisms, and rates of these processes is necessary to reproduce geodynamic processes in the lithosphere. For example, evaluating the *P–T* evolution of metamorphic rocks is importante for understanding the evolutionary histories of orogenic belts (Selverstone, 1985; Spear, 1993; Gerya et al., 2000; Jamieson et al., 2002; Waren et al., 2008). Metamorphic garnet, one of the principal minerals of metamorphic rocks, plays therein a very important role due to its chemical heterogeneity that "records", in certain situations, information on the *P–T* evolution of rocks (Florence and Spear, 1991; Evans, 2004; Caddick, 2010). This paper presents data on the heterogeneity of garnet that provides a key to understanding the metamorphic evolution of one of the central areas of the Central Asian Orogenic Belt (CAOB).

GEOLOGY

The Southern Altai Metamorphic Belt in western Mongolia (Fig. 1) extends submeridionally for more than 600 km along the Main Mongolian Suture, which separates the mostly Early Paleozoic domains in the northern part from the Late Paleozoic ones in the south (Tomurtogoo, 1997; Badarch et al., 2002; Windley et al., 2007). This tectonic setting makes the belt in the Mongolian Altai extremely important for understanding the collisional and orogenic processes. A number of geodynamic hypotheses were suggested to explain the origin of this structure (Ruzhentsev and Pospelov, 1992; Sengör et al., 1993; Mossakovskii et al., 1993; Badarch et al., 2002; Xiao et al., 2004; Windley et al., 2007), but no models for the magmatic processes has been put forth so far. According to (Badarch et al., 2002), this metamorphic belt composes the Tseel terrane, which separates an island-arc (Erden) and backarc (Gobi Altai) terranes (Fig. 1b). The Southern Altai Belt continues westward in complexes of the Chinese Altai, with which it is correlated in the age of the protolith and the timing and parameters of metamorphism (Jiang et al., 2012).

In spite of the key setting of this belt, the petrology of its metamorphic rocks is studied poorly, and their *P–T* paths have not been estimated. Analysis of folding and mineral assemblages in the belt indicates that it was affected by two contrasting types of metamorphism: older high-gradient metamorphism of the

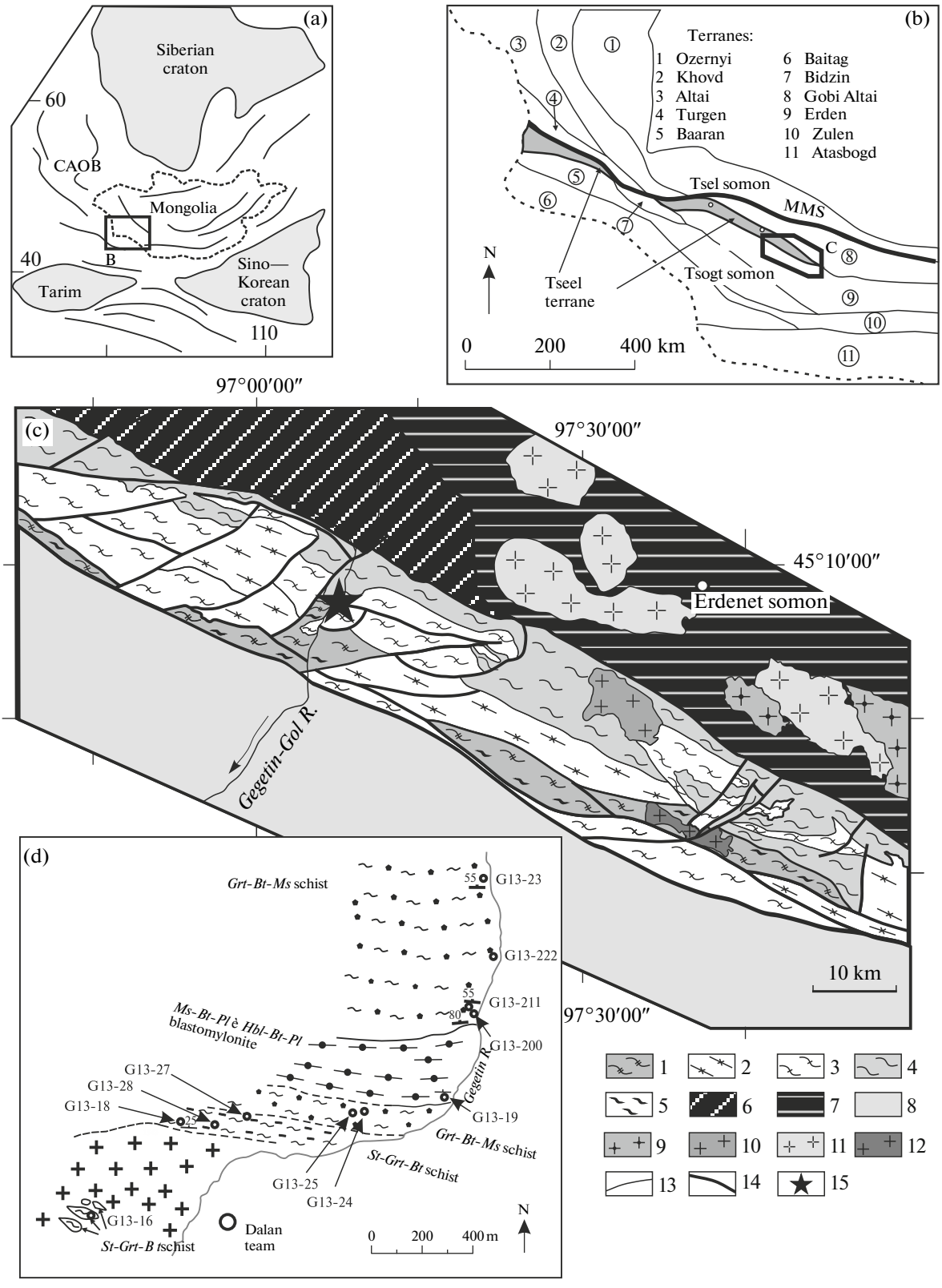
(a)
Siberian craton
60
CAOB
Mongolia
40
B
Tarim
Sino—Korean craton
110
(b)
Terranes:
1 Ozernyi
2 Khovd
3 Altai
4 Turgen
5 Baaran
6 Baitag
7 Bidzin
8 Gobi Altai
9 Erden
10 Zulen
11 Atasbogd
Tsel somon
MMS
C
N
Tseel terrane
Tsogt somon
0 200 400 km
97°00′00″
(c)
97°30′00″
45°10′00″
Erdenet somon
Gegetin-Gol R.
10 km
97°30′00″
(d)
Grt-Bt-Ms schist
G13-23
G13-222
G13-211
G13-200
Ms-Bt-Pl è Hbl-Bt-Pl blastomylonite
G13-27
G13-28
G13-18
G13-19
Gegetin R.
Grt-Bt-Ms schist
St-Grt-Bt schist
G13-25
G13-24
G13-16
St-Grt-B tschist
Dalan team
0 200 400 m
N
1 2 3 4
5 6 7 8
9 10 11 12
13 14 15

Fig. 1. (a) Location map of the study area in the Central Asian Orogenic Belt. (b) Schematic tectonic map of the Tsel terrane in southwestern Mongolia (after Badarch et al., 2002). MMS is the Main Mongolian Suture. (c) Schematic geological map of the Tsogt Block (modified from *Geological Map of the Mongolian People's Republic*, scale 1 : 200000, Sheets L-47-XXV and L-47-XXVI. (1–5) Metamorphic complexes of the Southern Altai Metamorphic Belt: (1) amphibolite; amphibole, biotite, biotite–amphibole, and biotite–muscovite crystalline schists and gneisses with garnet and, rarely, pyroxene, (2) variably migmatized biotite and biotite–amphibole gneisses and crystalline schists and amphibolite, (3) metasandstone, metasiltstone, and biotite–muscovite schists, sometimes containing garnet, cordierite, andalusite, sillimanite, and staurolite, (4) metabasalt, metandesite, metatuffite, metasandstone, amphibolite, and biotite and epidote–amphibole schists, sometimes with garnet and staurolite; biotite–sericite and sericite–chlorite schists; (5) migmatite; (6, 7) Caledonides in the marginal portion of the North Asian paleocontinent: (6) basalt, basaltic andesite, andesite, rhyolite; chlorite, epidote–, and sericite–chlorite schists; (7) sandstone, siltstone, clay shale, limestone, and gritstone; (8) Hercynides in the Southern Mongolian Belt; (9) Permian biotite and muscovite–biotite granite; (10) Devonian quartz monzonite and granosyenite; (11) mid-Devonian biotite and amphibole–biotite gneissose plagiogranite; (12) Devonian biotite and amphibole–biotite leucocratic granite; (13) boundaries of geological complexes; (14) tectonic boundaries; (15) location map of the area in Fig. 1d. (d) Geological map and sampling sites in the garnet and staurolite zones.

andalusite–sillimanite type and younger low-gradient metamorphism of the kyanite–sillimanite type (Kozakov, 1986; Bibikova, 1992; and others). This sequence of metamorphic episodes was confirmed by kyanite pseudomorphs after andalusite in the Tseel-somon area (Sukhorukov, 2007). At the same time, an episode of high-gradient (HT/LP) metamorphism was suggested in (Burenjargal et al., 2012, 2014) to occur after the metamorphism of the kyanite–sillimanite type, which is in conflict with earlier data. This paper reports newly obtained petrologic data that shed light on details of the tectonic evolution of the eastern portion of the Southern Altai Belt and make it possible to estimate its metamorphic evolutionary history.

Geologically, the study area is constrained to the Tsogt tectonic plate (Kozakov et al., 2007) in the Tsogt-somon area, in the basin of the Gegetin-Gol River (Fig. 1c). The area is dominated by aluminous schists metamorphosed to the greenschist and epidote-amphibolite facies that alternate with garnet amphibolite and rare intrusive granitoid bodies. In the south, the metamorphic schists occur in contact with a block of high-temperature migmatized feldspathic gneisses intercalating with garnet amphibolite. The granite gneiss was dated at 360 ± 1.1 Ma (Kroner et al., 2007). The block also hosts sheared granite and diorite intrusions dated at 295 ± 2.2 and 289 ± 2.3 Ma, reservoir (Kroner et al., 2007).

PETROGRAPHY, TEXTURE, AND CHEMICAL COMPOSITION OF THE ROCKS

The complex is dominated by aluminous schists, which localy interbeded with amphibolite. The metamorphic grade increases from north to south, and the following zones are distinguished according to their mineral assemblages: biotite–muscovite (*Bt* + *Ms* + *Chl* + *Ab* + *Qz*[1]), garnet (*Grt* + *Bt* + *Ms* + *Chl* + *Pl* + *Qz*), and staurolite (*St* + *Grt* ± *Ky* + *Bt* + *Ms* + *Chl* + *Pl* + *Qz*) (Table 1, Fig. 1d). The mineral composition of the amphibolites is represented by *Grt* + *Hbl* ± *Bt* + *Pl* + *Qz* assemblage.

[1] Here and below, mineral symbols are according to (Whitney and Evans, 2010).

The schists typically have a lepidoblastic texture, with garnet and staurolite porphyroblasts. The staurolite porphyroblasts are usually euhedral and host quartz and ilmenite inclusions, which are mostly oriented along a single direction that commonly does not coincides with the foliation of the rock (Fig. 2a). Muscovite often develops in "pressure shadows", which commonly occur at staurolite crystals, and on schistosity planes. The garnet occurs as a number of generations of different textural setting. One of these generations contains euhedral cores that host practically no mineral inclusions. These cores are surrounded by rims abounding in quartz, ilmenite, and carbonaceous-matter inclusions. The outermost zones are usually free of inclusions (Figs. 3d–3f). The garnet of the second population contains no cores and typically abounds in quartz and ilmenite inclusions, which sometimes define S-shaped and snowball trails (Figs. 2b, 3c, 3g). This garnet is also sometimes armored with rims devoid of mineral inclusions. The third garnet generation occurs as hopper crystals around cores, wich have no contact with one another

Table 1. Mineralogical composition of schist in the Gegetin area

Sample	*St*	*Grt*	*Bt*	*Ms*	*Chl*	*Hbl*	*Pl*	*Qz*
G-13-09				+	+			+
G-13-10				+	+			+
G-13-20		+	+		+		+	+
G-13-20-0		+	+	+	+		+	+
G-13-21		+	+		+	+	+	+
G-13-21-1		+	+		+		+	+
G-13-22		+	+	+			+	+
G-13-23		+	+	+	+		+	+
G-13-26		+	+				+	+
G-13-16	+	+	+	+			+	+
G-13-18	+	+	+	+			+	+
G-13-25	+	+	+	+			+	+
G-13-26-1	+	+	+				+	+
G-13-27	+	+	+	+			+	+
G-13-29	+	+	+	+			+	+

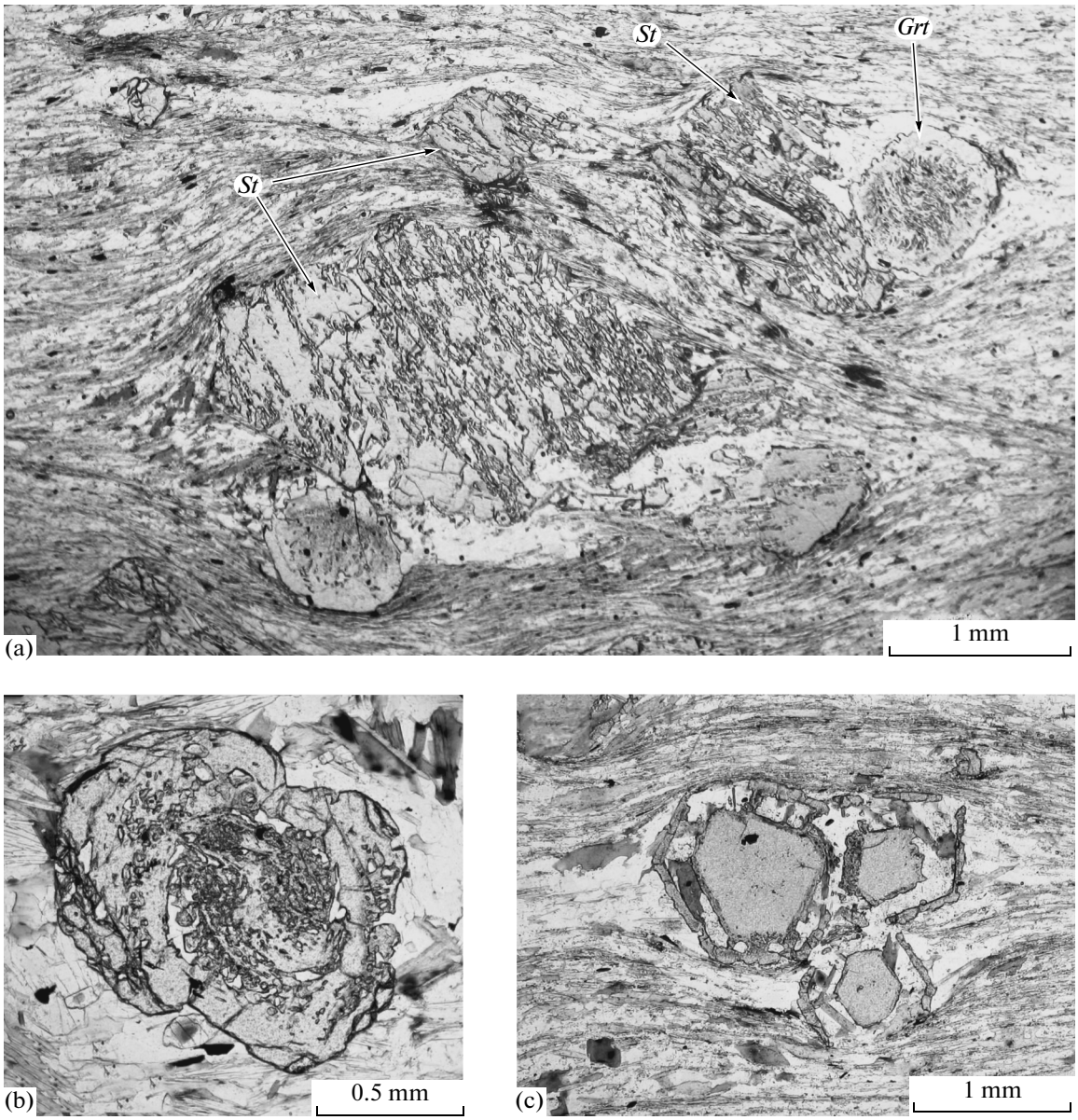

Fig. 2. Micrographs of thin sections of the aluminous schists. (a) Inclusion trails in staurolite and garnet porphyroblasts; (b) snowball-structure in a garnet crystal; (c) garnet hopper crystals (outer zones).

at all or occurring only at a few points (Fig. 2c). The inner and outer zones are separated by matrix minerals, first and foremost, by quartz, biotite, and ilmenite. Sometimes the outer zones develop immediately around the cores, and intermediate zones are absent. The porphyroblasts are often accompanied by pressure shadows.

The bulk chemistry of the rocks was analyzed by XRF at the Sobolev Institute in Novosibirsk. The aluminous schists contain broadly varying SiO_2 concentrations, from 58 to 67 wt % (Table 2). In the $MgO/CaO–P_2O_5/TiO_2$ diagram (Fig. 4), they plot in the field of pararocks, and their metasedimentary nature also follows from their high Al_2O_3 concentrations (14–19 wt %) and the occurrence of aluminous minerals (staurolite and garnet) in these rocks. In the classification diagram (Herron, 1988), most of the composition points fall within the field of aluminous schists, and a single data point plots within the wacke field (Fig. 5).

MINERAL CHEMISTRIES AND TYPES OF GARNET ZONING

We have studied rock samples from various metamorphic zones, which are characterized by distinct types of the chemical heterogeneity of their garnet. The samples from the garnet zone are G-13-222,

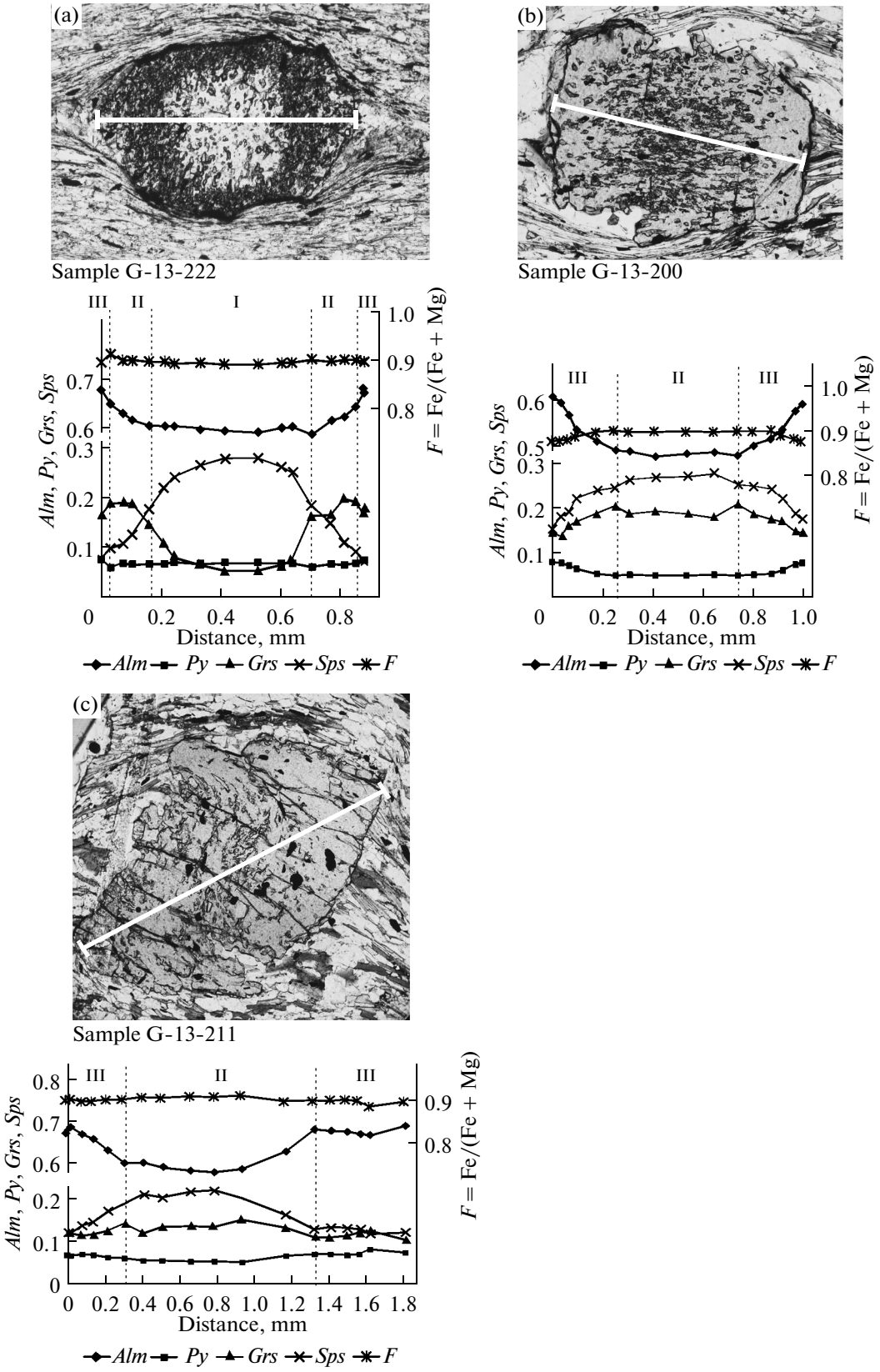

Fig. 3. Micrographs of and concentration profiles across garnet grains from (a, b, and c) the garnet and (d, e, f, and g) staurolite zones. (a) Sample G-13-222, (b) sample G-13-200, (c) sample G-13-211, (d) sample G-13-16, (e) sample G-13-16a, (f) sample G-13-18, (g) sample G-13-27. In concentration profiles, dotted lines mark the probable boundaries between the first-, second- and third-population garnet (denoted I, II, and III, respectively).

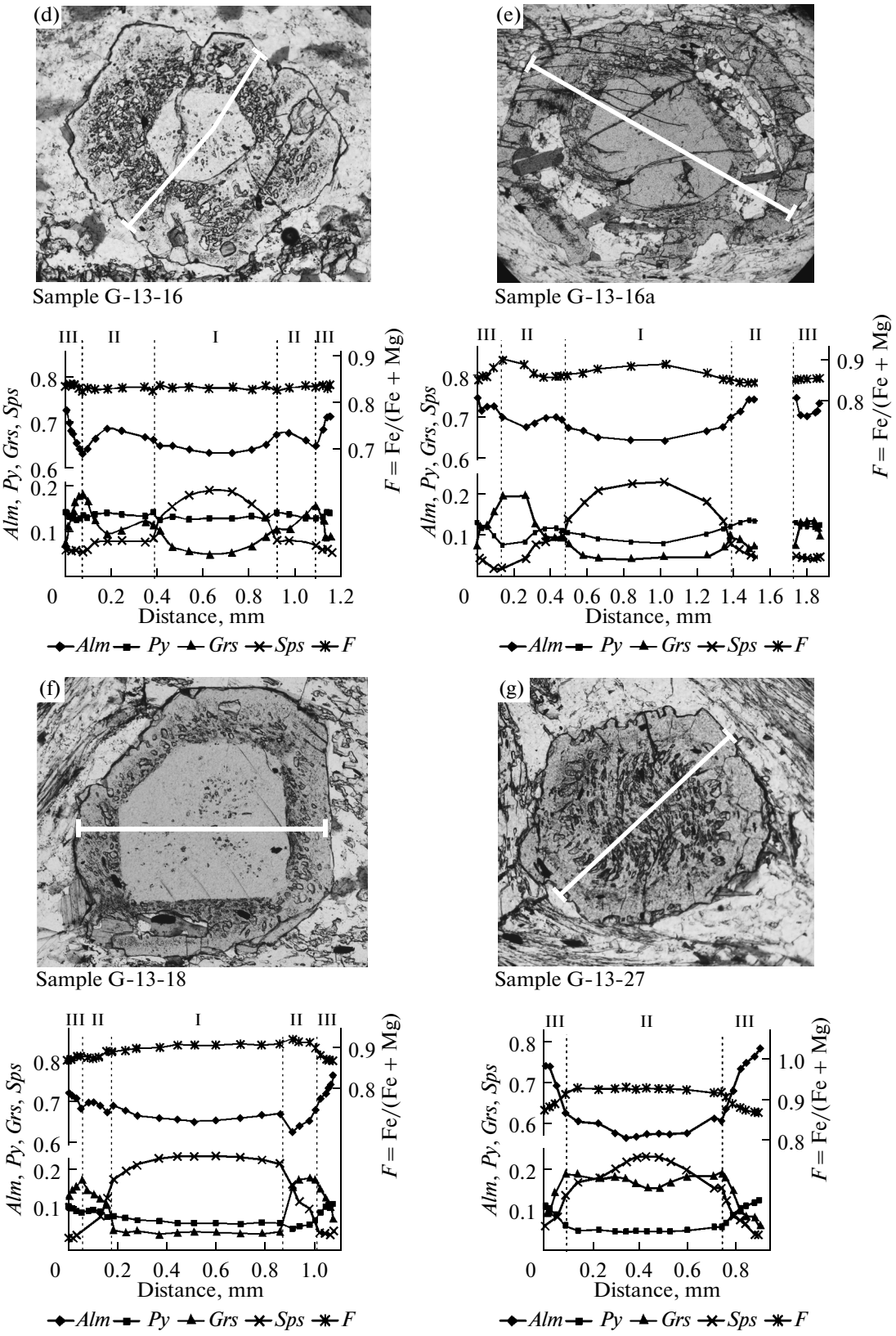
(d)
(e)
Sample G-13-16
Sample G-13-16a
III II I II III
Alm, Py, Grs, Sps
F = Fe/(Fe + Mg)
Distance, mm
Alm Py Grs Sps F
(f)
(g)
Sample G-13-18
Sample G-13-27

Fig. 3. (Contd.)

Table 2. Concentrations (wt %) of major oxides in aluminous schists in the Tsogt block

Component	G-13-18	G-13-20	G-13-200	G-13-211	G-13-222	G-13-27
SiO_2	60.33	63.04	67.87	57.96	61.69	64.10
TiO_2	0.69	0.73	0.64	0.99	0.76	0.74
Al_2O_3	19.04	16.60	14.28	18.19	17.24	18.04
Fe_2O_3	7.59	6.32	5.68	8.85	6.60	7.03
MnO	0.17	0.11	0.12	0.25	0.12	0.13
MgO	2.85	3.37	3.19	3.58	2.87	2.61
CaO	1.74	2.32	1.64	2.57	1.95	1.07
Na_2O	1.49	2.84	2.30	3.50	1.57	1.65
K_2O	3.02	2.64	2.42	1.66	3.65	3.32
P_2O_5	0.21	0.13	0.10	0.28	0.18	0.16
BaO	0.07	0.05	0.05	0.15	0.06	0.06
SO_3	<0.03	<0.03	<0.03	<0.03	<0.03	<0.03
V_2O_5	0.019	0.016	0.015	0.024	0.017	0.018
Cr_2O_3	0.014	0.016	0.018	0.003	0.011	0.010
NiO	0.067	0.032	0.007	<.003	0.008	0.008
LOI	2.28	1.59	1.37	2.06	2.41	1.58
Total	99.62	99.85	99.77	100.13	99.18	100.59

G-13-200, and G-13-211; and those form the staurolite zone are G-13-27, G-13-22, G-13-16, and G-13-18.

Garnet Zone

Sample G-13-222 (Fig. 3a). The garnet grains are approximately 0.5 mm across and have a complicated inner structure. Their cores are devoid of mineral inclusions and are surrounded by rims with abundant quartz and ilmenite inclusions. The compositions of the cores and rims are principally different. The cores are poorer in grossular and almandine than the rims. The composition of the cores is *Alm* 0.59–0.60, *Prp* 0.07, *Grs* 0.05–0.16, *Sps* 0.28–0.18; and that of the rims is *Alm* 0.60–0.68, *Prp* 0.06–0.07, *Grs* 0.16–0.19, *Sps* 0.07–0.18 (Table 3).

Sample G-13-200 (Fig. 3b). The garnet zoning is analogous to that in sample G-13-211, but inclusions in the core are oriented linearly. The garnet has a composition *Alm* 0.47–0.61, *Prp* 0.05–0.08, *Grs* 0.14–0.20, *Sps* 0.27–0.15. The biotite contains 1.4–1.5 wt % TiO_2 and 0.41–0.46 f.u. Al(VI). The plagioclase contains 0.25–0.27 *An*.

Sample G-13-211 (Fig. 3c). The garnet does not contain cores, but the zoned distribution of the *Sps* concentration is quite obvious. The garnet grains contain quartz and ilmenite inclusions that form S-shaped trails due to rotation of the host crystals. The composition of the garnet is *Alm* 0.58–0.69, *Prp* 0.05–0.08, *Grs* 0.15–0.10, *Sps* 0.22–0.12. The grossular and spessartine concentrations reach a maximum in the central part of garnet grains and decrease toward rims. Conversely, the pyrope and almandine concentrations increase toward the rims. The composition of the rims is *Alm* 0.69, *Prp* 0.08, *Grs* 0.11, *Sps* 0.12. The biotite contains 1.47 wt % TiO_2, and the plagioclase contains 0.16–0.18 *An* (Table 4).

Staurolite Zone

Sample G-13-16 (Figs. 3d, 3e, 6). Garnet in this sample has the most complicated type of its zoning. The central parts of the grains contain euhedral cores, which are clearly seen under an optical microscope because they contain practically no mineral inclusions. The cores are surrounded by garnet rims containing inclusions mostly of quartz, ilmenite, and carbonaceous matter. The outer rims are hopper crystals that either do not touch the core or touch them only at

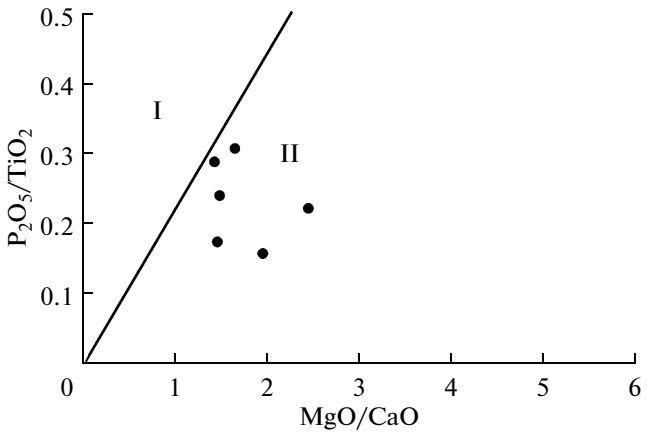

Fig. 4. MgO/CaO–P_2O_5/TiO_2 diagram for the aluminous schists. Fields (Werner, 1986): (I) orthorocks, (II) pararocks.

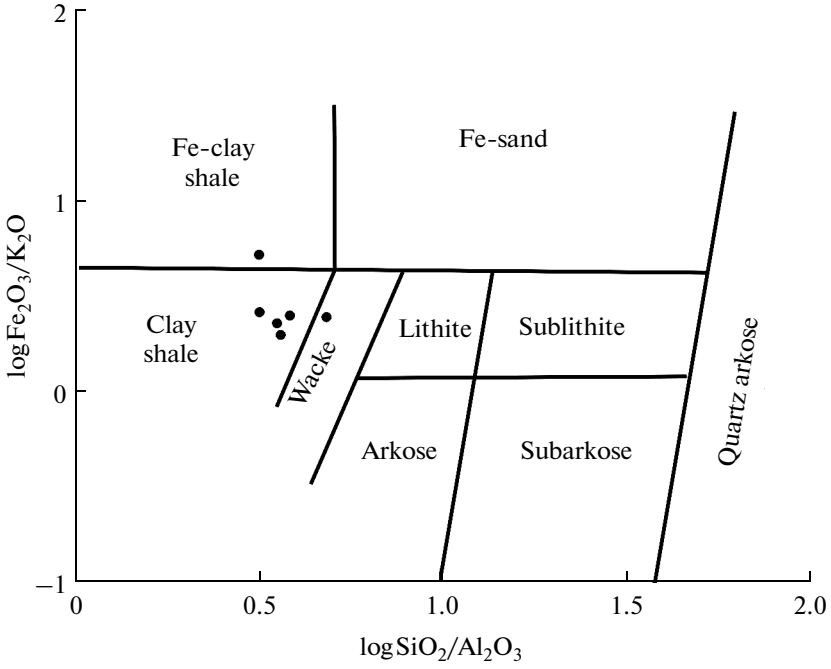

Fig. 5. Herron (1988) diagram for terrigenous rocks showing the composition of the aluminous schists.

a few points. The cores contain 0.188–0.08 *Sps*, and its concentration gradually decreases toward the rims. The *Grs* concentration conversely increases from core to margin: *Grs* 0.05–0.12. The pyrope concentration varies insignificantly, *Prp* 0.12–0.13; and the concentration of almandine increases toward the margins, *Alm* 0.63–0.67. In the rims around the cores, the grossular concentrations are lower, *Grs* 0.12–0.09, and those of almandine are higher, *Alm* 0.67–0.68; the spessartine and pyrope concentrations remain practically unchanging, *Sps* 0.08, *Prp* 0.14. The third zone is characterized by a sharp increase in the grossular concentration to *Grs* 0.18–0.20 and a decrease in the concentrations of other end members to *Alm* 0.63, *Prp* 0.12, and *Sps* 0.05. The fourth, outermost, zone is poorer in grossular (*Grs* 0.07), richer in almandine and pyrope (*Alm* 0.72 and *Prp* 0.14), and possesses an unchanging spessartine concentration.

The composition of the biotite is practically the same in the rock matrix and in inclusions in garnet: the mineral contains 1.55–1.63 wt % TiO_2 and 0.40–0.49 f.u. Al(VI). The plagioclase is *An* 0.30–0.42 (Table 5).

Sample G-13-18 (Fig. 3f). The garnet grains bear Mg-rich cores poor in grossular, *Alm* 0.65–0.68, *Prp* 0.06–0.08, *Grs* 0.05, *Sps* 0.23–0.17. In the rim, the grossular concentration first sharply increases to *Grs* 0.17 and then decreases to *Grs* 0.073, and the almandine concentration simultaneously decreases to *Alm* 0.62 and then increases to *Alm* 0.76. The biotite contains 1.42–1.61 wt % TiO_2 and 0.42–0.43 f.u. Al(VI). The plagioclase is *An* 0.25–0.27. The staurolite has Fe# = 0.78–0.80 and contains 0.2 wt % ZnO.

Sample G-13-27 (Fig. 3g). The central portions of garnet grains abound in quartz and ilmenite inclusions, which compose S-shaped trails, and the outer rims bear no inclusions. In the central parts, the grossular concentration gently increases toward the rim, *Grs* 0.15–0.17, and the pyrope and almandine concentrations remain practically unchanging: *Alm* 0.56–0.60, *Prp* 0.04. In the rims (devoid of inclusions), the grossular concentration decreases to *Grs* 0.06, and the almandine and pyrope concentrations simultaneously increase to *Alm* 0.77, *Prp* 0.12. The Mn concentration gradually decreases from grain cores to rims, *Sps* 0.03–0.22. The biotite contains 1.6–1.7 wt % TiO_2 and 0.41–0.43 f.u. Al(VI). The plagioclase is *An* 0.19–0.20. The staurolite contains 0.28 wt % ZnO.

The types of garnet zoning described above led us to distinguish three successive garnet generations. The oldest one occurs in the cores of garnet grains and is characterized by the lowest grossular concentrations and high pyrope and almandine contents. The second generation, which usually contains mineral inclusions, typically possesses elevated grossular contents, and its spessartine concentrations depend on whether the garnet of this generation surrounds an older core or forms a core of garnet grain itself. The garnet of the third generation shows variable grossular, pyrope, and almandine concentrations and contains the lowest spessartine concentrations because always forms the outermost zones of crystals of sheath crystals. The ternary MnO–CaO–FeO diagram (Fig. 7) illustrates the composition of the garnet of various generations.

Table 3. Composition (wt %) of garnet grains in aluminous schists from the Gegetin area that were used in our calculations and are plotted in the *P-T* diagrams

Component	G-13-222			G-13-211		G-13-200		G-13-16							G-13-18				G-13-27		
	I	II	III	II	III	II	III	I	IIc	IIi	III	a	b	c	I	IIc	IIi	III	IIc	IIi	III
SiO_2	37.13	62.52	36.86	37.05	37.31	37.34	37.40	36.84	37.68	37.23	37.35	37.07	37.14	37.14	36.67	37.32	37.43	37.18	36.78	36.79	37.27
TiO_2	–	–	–	–	–	–	–	–	–	–	–	–	–	–	–		–	–	–	–	–
Al_2O_3	20.71	16.39	20.70	20.53	20.74	20.71	20.77	20.69	20.78	20.93	21.19	21.20	20.95	20.93	20.53	20.72	20.85	20.82	20.49	20.35	20.79
Cr_2O_3	–	–	–	–	–	–	–	–	–	–	–	–	–	–	–		–	–	–	–	–
FeO	26.43	21.07	29.98	26.35	30.99	21.83	27.58	28.41	30.75	31.47	31.92	31.66	31.38	32.02	29.33	28.11	31.34	32.78	25.06	28.22	32.73
MnO	11.57	3.21	3.41	9.13	5.50	11.53	6.94	10.14	3.49	1.11	1.83	2.53	2.79	2.60	10.36	7.31	2.10	1.44	9.95	5.40	2.62
MgO	1.70	1.09	1.92	1.37	1.94	1.32	2.09	2.02	2.74	1.96	3.07	3.14	3.40	3.42	1.74	1.39	2.43	2.81	1.13	1.67	2.68
CaO	2.27	4.79	5.70	5.45	3.77	7.51	5.22	1.67	4.6	7.06	4.63	4.11	4.01	3.57	1.67	5.46	6.24	4.83	5.25	6.23	3.19
Na_2O	–	–	–	–	–	–	–	–	–	–	–	–	–	–	–	–	–	–	–	–	–
K_2O	–	–	–	–	–	–	–	–	–	–	–	–	–	–	–	–	–	–	–	–	–
Total	99.85	109.19	98.58	99.89	100.25	100.28	100.10	99.84	100.1	99.81	100.03	99.75	99.74	99.73	100.41	100.4	100.46	99.95	98.76	98.77	99.32
Cations per 12O																					
Si	3.015	4.139	3.004	3.003	3.009	2.999	3.006	2.998	3.018	2.993	2.988	2.978	2.984	2.986	2.984	3.005	2.992	2.989	3.011	3.002	3.015
Ti	–	–	–	–	–	–	–	–	–	–	–	–	–	–	–	–	–	–	–	–	–
Al	1.982	1.279	1.988	1.961	1.972	1.961	1.968	1.984	1.962	1.983	1.998	2.007	1.984	1.983	1.969	1.967	1.965	1.973	1.977	1.957	1.982
Cr	–	–	–	–	–	–	–	–	–	–	–	–	–	–	–	–	–	–	–	–	–
Fe	1.795	1.167	2.043	1.786	2.090	1.466	1.854	1.933	2.060	2.116	2.136	2.127	2.109	2.153	1.996	1.893	2.095	2.204	1.716	1.926	2.214
Mn	0.796	0.180	0.235	0.627	0.376	0.784	0.472	0.699	0.237	0.076	0.124	0.172	0.190	0.177	0.714	0.499	0.142	0.098	0.690	0.373	0.180
Mg	0.205	0.108	0.233	0.165	0.233	0.157	0.250	0.245	0.327	0.235	0.366	0.376	0.407	0.410	0.211	0.167	0.289	0.337	0.138	0.203	0.324
Ca	0.197	0.340	0.498	0.473	0.326	0.646	0.450	0.146	0.395	0.608	0.397	0.354	0.345	0.308	0.145	0.471	0.535	0.416	0.460	0.545	0.276
Na	–	–	–	–	–	–	–	–	–	–	–	–	–	–	–	–	–	–	–	–	–
K	–	–	–	–	–	–	–	–	–	–	–	–	–	–	–	–	–	–	–	–	–
End members																					
Alm	0.60	0.65	0.68	0.59	0.69	0.48	0.61	0.64	0.68	0.70	0.71	0.70	0.69	0.71	0.65	0.62	0.68	0.72	0.57	0.63	0.74
Prp	0.07	0.06	0.08	0.05	0.08	0.05	0.08	0.08	0.11	0.08	0.12	0.12	0.13	0.13	0.07	0.06	0.09	0.11	0.05	0.07	0.11
Grs	0.07	0.19	0.17	0.16	0.11	0.21	0.15	0.05	0.13	0.20	0.13	0.12	0.11	0.10	0.05	0.16	0.17	0.14	0.15	0.18	0.09
Sps	0.27	0.10	0.08	0.21	0.12	0.26	0.16	0.23	0.08	0.02	0.04	0.06	0.06	0.06	0.23	0.16	0.05	0.03	0.23	0.12	0.06
F	0.90	0.92	0.90	0.92	0.90	0.90	0.88	0.89	0.86	0.90	0.85	0.85	0.84	0.84	0.90	0.92	0.88	0.87	0.93	0.90	0.87

I, II, and III are garnet generations; IIc is an analysis of second-generation garnet closer to the grain center, IIi is the intermediate zone, a, b, and c are analyses of hopper garnet crystals, $F = Fe/(Fe + Mg)$.

Table 4. Composition (wt %) of minerals other than garnet in aluminous schists of the garnet zone

Component	G-13-200					G-13-22				G-13-20					G-13-222				G-13-211			
	Bt	*Ms*	*Chl*	*Plc*	*Plr*	*Bt*	*Ms*	*Plc*	*Plr*	*Bt*	*Chl*	*Ms*	*Plc*	*Plr*	*Bt*	*Ms*	*Plc*	*Plr*	*Bt*	*Chl*	*Plc*	*Plr*
SiO_2	37.39	47.35	28.68	61.52	61.18	36.45	48.58	59.97	58.99	36.82	23.82	49.02	62.24	62.03	36.85	48.61	59.08	58.98	36.71	24.30	67.41	68.14
TiO_2	1.51	0.36	0.32	–	–	2.17	0.59	–	–	1.72	0.08	0.42	–	–	1.46	0.23	–	–	1.47	0.13	–	–
Al_2O_3	18.63	34.21	22.09	24.11	24.52	18.91	35.13	25.14	25.93	18.46	23.70	33.34	23.74	23.55	18.17	33.09	25.51	25.53	18.09	22.38	21.81	21.35
Cr_2O_3	–	–	–	–	–	–	–	–	–	–	–	–	–	–	–	–	–	–	–	–	–	–
FeO	16.62	1.16	21.69	0.13	0.10	16.87	0.81	0.06	0.05	16.64	22.01	1.15	0.04	0.03	18.37	1.95	0.12	0.11	19.68	26.48	0.02	0.03
MnO	0.15	0.01	0.22	–	–	0.08	0.00	–	–	0.15	0.26	0.00	–	–	0.11	0.02	–	–	0.09	0.18	–	–
MgO	12.03	1.07	16.28	–	–	11.32	0.64	–	–	11.67	17.98	1.05	–	–	10.42	1.46	–	–	10.23	14.74	–	–
CaO	-	-	-	5.56	5.98	–	–	6.92	7.76	–	–	–	5.31	5.43	–	–	7.51	7.41	–	–	2.89	2.56
Na_2O	0.20	0.82	0.02	8.74	8.51	0.34	1.05	7.57	7.31	0.15	0.02	0.65	8.46	8.58	0.07	0.49	7.67	7.61	0.33	0.03	7.46	7.37
K_2O	8.67	9.85	1.22	0.11	0.09	8.74	9.39	0.07	0.07	9.77	0.01	9.92	0.09	0.09	9.81	9.84	0.10	0.10	9.25	0.01	0.07	0.07
H_2O	4.50	4.50	10.00	–	–	4.50	4.50	–	–	4.50	12.00	4.50	–	–	4.50	4.50	–	–	4.50	12.00	–	–
Total	99.79	99.37	100.55	100.23	100.41	99.43	100.67	99.79	100.15	99.90	99.92	100.11	99.88	99.71	99.80	100.21	100.04	99.75	100.45	100.36	99.67	99.53
Numbers of cations were normalized to 11O for *Bt* and *Ms*. 8O for *Pl*, and 18O for *Chl*																						
Si	2.783	3.149	3.679	2.729	2.711	2.735	3.166	2.676	2.631	2.761	3.172	3.226	2.760	2.758	2.788	3.208	2.641	2.642	2.771	3.294	2.934	2.962
Ti	0.084	0.018	0.031	–	–	0.122	0.029	–	–	0.097	0.008	0.021	–	–	0.083	0.011	–	–	0.083	0.013	–	–
Al	1.635	2.682	3.340	1.261	1.281	1.672	2.699	1.322	1.363	1.632	3.720	2.586	1.240	1.234	1.621	2.575	1.344	1.348	1.609	3.577	1.119	1.094
Cr	–	–	–	–	–	–	–	–	–	–	–	–	–	–	–	–	–	–	–	–	–	–
Fe	1.035	0.064	2.327	0.005	0.004	1.059	0.044	0.002	0.002	1.043	2.452	0.063	0.001	0.001	1.163	0.108	0.004	0.004	1.243	3.002	0.001	0.001
Mn	0.009	0.001	0.024	–	–	0.005	0.000	–	–	0.010	0.030	0.000	–	–	0.007	0.001	–	–	0.005	0.021	–	–
Mg	1.335	0.106	3.112	–	–	1.266	0.062	–	–	1.304	3.568	0.103	–	–	1.175	0.144	–	–	1.151	2.978	–	–
Ca	–	–	–	0.264	0.284	–	–	0.331	0.371	–	–	–	0.252	0.259	–	–	0.359	0.356	–	–	0.135	0.119
Na	0.029	0.105	0.006	0.752	0.731	0.049	0.132	0.655	0.633	0.022	0.004	0.083	0.727	0.739	0.010	0.063	0.665	0.661	0.049	0.008	0.629	0.621
K	0.824	0.836	0.199	0.006	0.005	0.836	0.781	0.004	0.004	0.934	0.002	0.833	0.005	0.005	0.947	0.828	0.005	0.006	0.891	0.002	0.004	0.004
F	0.44		0.43			0.46				0.44	0.41				0.50				0.52	0.50		
End members																						
An				0.26	0.28			0.33	0.37				0.26	0.26			0.35	0.35			0.18	0.16
Ab				0.74	0.72			0.66	0.63				0.74	0.74			0.65	0.65			0.82	0.83
Or				0.01	0.00			0.00	0.00				0.01	0.01			0.01	0.01			0.00	0.01

Plc and *Plr* are plagioclase analyses in grain cores and rims.

Table 5. Composition (wt %) of minerals other than garnet in aluminous schists of the staurolite zone

Component	G-13-18					G-13-16					G-13-27					
	St	*Bt*	*Ms*	*Plc*	*Plr*	*St*	*Bt*	*Ms*	*Plc*	*Plr*	*St*	*Bt*	*Ms*	*Chl*	*Plc*	*Plr*
SiO_2	24.93	37.02	47.58	60.88	61.23	26.39	36.48	47.09	57.33	57.98	24.47	36.61	50.06	24.07	64.05	63.95
TiO_2	0.60	1.42	0.48	–	–	0.53	1.56	0.55	–	–	0.37	1.73	0.37	0.13	–	–
Al_2O_3	56.74	19.14	35.16	24.10	23.96	55.41	18.96	34.84	26.08	26.61	57.61	19.03	33.90	24.11	23.11	22.83
Cr_2O_3	0.00	–	–	–	–	0.00	–	–	–	–	0.00	–	–	–	–	–
FeO	13.74	17.49	0.93	0.15	0.18	12.61	16.43	0.90	0.05	0.05	13.89	18.43	0.94	23.99	0.08	0.07
MnO	0.17	0.04	0.00	–	–	0.21	0.03	0.00	–	–	0.10	0.02	0.02	0.04	–	–
MgO	1.81	11.28	0.64	–	–	1.77	12.20	0.86	–	–	1.73	10.85	0.86	16.19	–	–
CaO	–	–	–	5.43	5.57	–	–	–	8.38	8.77	–	–	–	–	4.24	4.10
Na_2O	0.02	0.48	1.23	8.66	8.52	0.00	0.20	1.18	7.30	6.97	0.02	0.45	1.47	0.03	8.96	9.12
K_2O	0.00	9.26	9.76	0.07	0.07	0.00	9.05	9.69	0.06	0.07	0.01	8.92	8.77	0.02	0.06	0.05
ZnO	0.21	–	–	–	–	0.53	–	–	–	–	0.28	–	–	–	–	–
H_2O	2.00	4.50	4.50	–	–	2.00	4.50	4.50	–	–	2.00	4.50	4.50	12.00	–	–
Total	100.23	100.68	100.36	99.29	99.57	99.55	99.50	99.64	99.19	100.51	100.48	100.53	100.88	100.59	100.58	100.12
Numbers of cations were normalized on 11O for *Bt* and *Ms*, 8O for *Pl*, 18O for *Chl*, and 48O for *St*																
Si	6.624	2.753	3.129	2.725	2.732	7.025	2.732	3.121	2.593	2.586	6.492	2.736	3.245	3.203	2.809	2.818
Ti	0.12	0.080	0.024	–	–	0.106	0.088	0.027	–	–	0.074	0.097	0.018	0.013	–	–
Al	17.77	1.678	2.725	1.271	1.260	17.38	1.674	2.721	1.390	1.399	18.01	1.676	2.590	3.783	1.195	1.185
Cr	0	–	–	–	–	0	–	–	–	–	0	–	–	–	–	–
Fe	3.053	1.088	0.051	0.006	0.007	2.807	1.029	0.050	0.002	0.002	3.082	1.152	0.051	2.671	0.003	0.002
Mn	0.038	0.002	0.000	–	–	0.047	0.002	0.000	–	–	0.022	0.001	0.001	0.005	–	–
Mg	0.717	1.250	0.062	–	–	0.702	1.362	0.085	–	–	0.684	1.208	0.083	3.211	–	–
Ca	–	–	–	0.260	0.266	–	–	–	0.406	0.419	–	–	–	–	0.199	0.193
Na	–	0.070	0.157	0.752	0.737	–	0.028	0.152	0.640	0.603	–	0.065	0.185	0.009	0.762	0.779
K	–	0.878	0.819	0.004	0.004	–	0.864	0.819	0.004	0.004	–	0.850	0.725	0.004	0.003	0.003
Zn	0.041	–	–	–	–	0.104	–	–	–	–	0.055	–	–	–	–	–
F	0.81	0.47				0.80	0.43		0.39	0.41	0.82	0.49		0.45		
End members																
An				0.74	0.73				0.61	0.59					0.79	0.80
Ab				0.00	0.00				0.00	0.00					0.00	0.00
Or				0.00	0.00				0.00	0.00					0.00	0.00

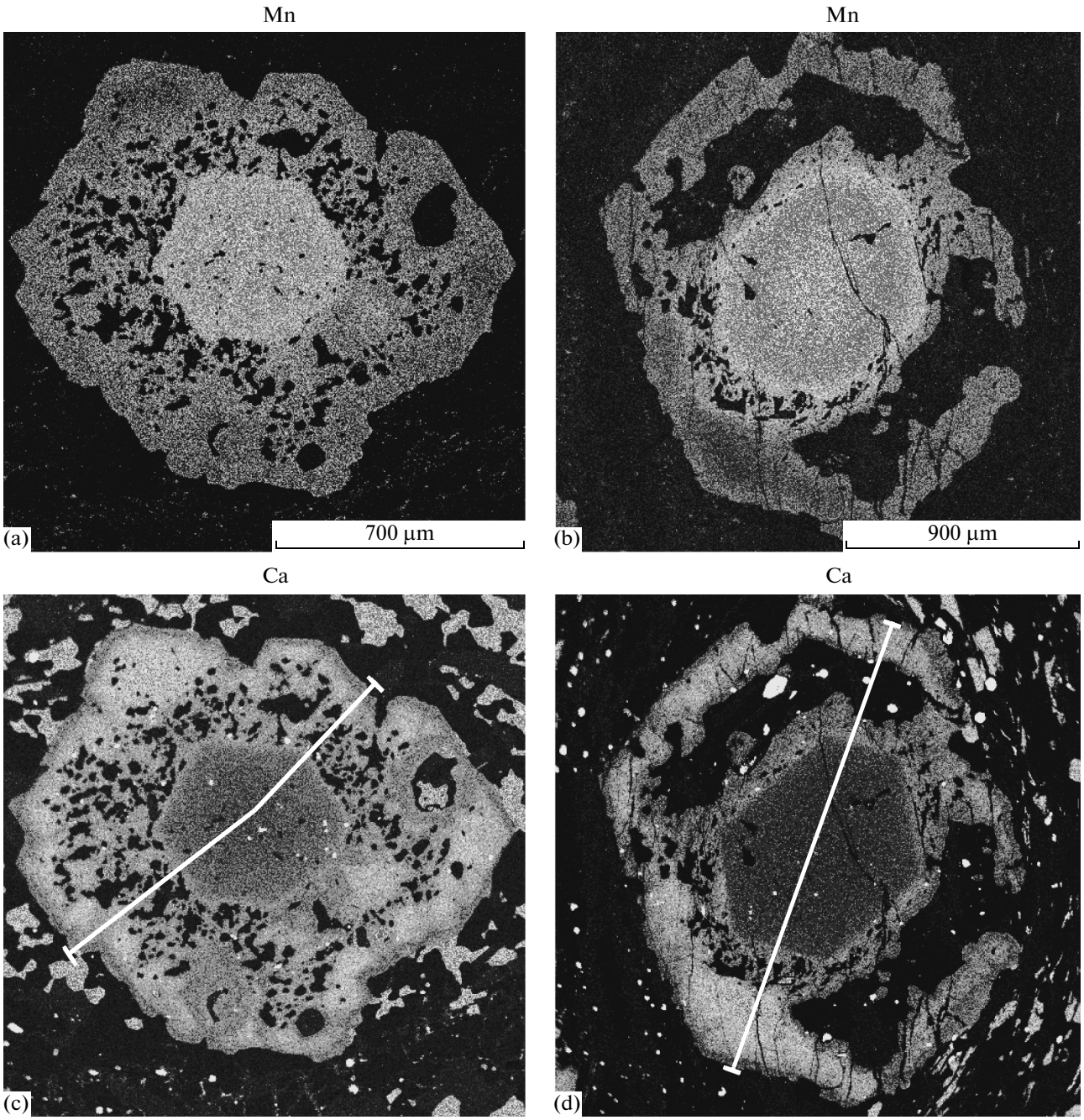

Fig. 6. Distribution of (a, b) Mn and (c, d) Ca in garnet grains in sample G-13-16. BSE images. The concentration profiles marked by lines are shown in Figs. 3d and 3e.

P–T PARAMETERS OF METAMORPHISM

Zoned garnet grains were successfully utilized to estimate the thermal evolution of several metamorphic complexes worldwide (Perchuk et al., 1985; Aranovich, 1991; Spear, 1993; Kohn, 2005; Caddick et al., 2010). To do this, some researchers estimated the *P–T* parameters by mineralogical geothermomethers and geobarometers, using mineral inclusions in various growth zones of garnet grains. This technique was applied, for example, to calculate the *P–T–t* path of metamorphism in the Yenisei Range (Likhanov et al., 2013). In the absence of such inclusions, the most efficient approach is to construct phase diagrams (pseudosections) and evaluate the *P–T* parameters from intersections of composition isopleths (Caddick and Kohn, 2013).

To estimate the *P–T* metamorphic parameters and reproduce the thermal history of aluminous schists in the Getegin-Gol area, we applied, on the one hand,

mineralogical geothermometers and geobarometers [garnet–biotite (GB) (Holdaway, 2000) and garnet–biotite–plagioclase–quartz (GBPQ) (Wu, 2004)] and, on the other hand, used the Perplex 668 software (Connolly, 1990, 2009). The application of mineralogical geothermometers in rocks bearing minerals of significantly heterogeneous composition is limited because it is not known which zones of the minerals were in equilibrium with one another at certain moments of time. In view of this, geothermometers were used to estimate the crystallization conditions only for equilibria between the outermost garnet zones and matrix minerals and to compare these parameters estimated from intersections of composition isopleths. The technique of constructing phase diagrams (pseudosections) is underlain by minimizing the Gibbs free energy and makes it possible to calculate the *P–T* stability fields of equilibrium mineral associations (Connoly, 1990). Moreover, known garnet compositions can be plotted in these diagrams as isopleths, whose intersections indicate the *P–T* parameters of the mineral equilibria. An advantage of this technique is that the calculations can involve all phases that are present in the rock and exchanged components with one another. This technique also makes it possible not only to quantify the temperature and pressure but also to evaluate the evolution of the crystallization *P–T* parameters of the garnet grains.

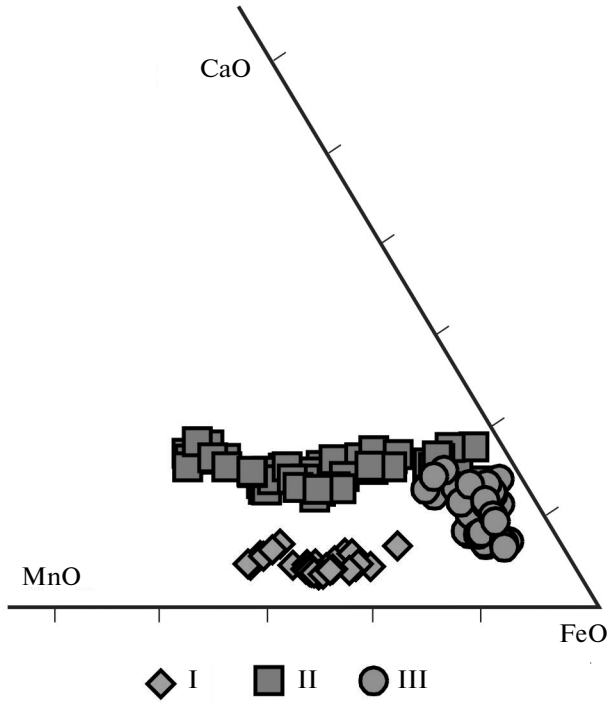

Fig. 7. MnO–CaO–FeO diagram for the composition of the first, second, and third (I, II, and III, respectively) garnet populations.

One of the principal assumptions made when this approach is applied is that the rims of a growing garnet grain were in equilibrium with the rock matrix, which allows one to further assume that the composition of the garnet was essentially controlled by the temperature and pressure. Garnet grows in low- and medium-grade metamorphic rocks mostly because of dehydration reactions, which produce excess H_2O-rich fluid and thus facilitate reaching equilibrium (Carlson, 1989, 2001; Dohmen and Chakraborty, 2003). Another assumption is that the original growth profiles across the garnet grains are preserved and have not been modified by intragranular diffusion. The rates of diffusion processes are controlled first of all by temperature and are believed to be negligibly low for garnet grains in rocks metamorphosed at parameters lower than the amphibolite facies (Chakraborty, Ganguly, 1992; Ayres and Vance, 1997). The isopleth technique was earlier successfully applied in studying complexes affected by a single episode of metamorphism (Menard and Spear, 1993; Stowell et al., 2001; Evans, 2004; Kim and Bell, 2005) and polymetamorphic ones (Zeh et al., 2004).

We have constructed phase diagrams for samples from the garnet and staurolite zones, whose garnet grains show different types of their chemical heterogeneity. The simulations were carried out in the Na_2O–CaO–K_2O–FeO–MgO–MnO–Al_2O_3–SiO_2–TiO_2 (NCKFMMnAST) system, with fluid saturated with H_2O, at $P = 2$–10 kbar and $T = 500$–700°C. We used models for solid solutions for garnet, chlorite, muscovite, and staurolite according to (Holland and Powell, 1998), plagioclase according to (Newton et al., 1980), and biotite according to (Tajcmanova et al., 2009). Geological observations allowed us to reject melt from our considerations, the *P–T* parameters were determined by the intersections of grossular, spessartine, and almandine.

RESULTS

Garnet Zone

The garnet stability field covers practically the whole *P–T* region shown in the diagram (Fig. 8). The intersection of isopleths for all samples from the garnet zone lies in the field of the *Grt* + *Bt* + *Ms* + *Chl* + *Pl* + *Qz* + *Ilm* mineral assemblage, which is consistent with what is observed in the thin sections. In this area, all grossular isopleths have positive slopes close to 45° in *P–T* space, the pyrope and almandine isopleths are almost perpendicular to the temperature axis, the almandine content increases with temperature, and the spessartine content increases with increasing temperature and pressure.

Sample G-13-222 (Fig. 8a). The *P–T* parameters inferred from isopleth intersection for the core of a garnet grain are $T = 545$°C, $P = 3.7$ kbar. For the surrounding rim, which is rich in quartz inclusions, the pressure is notably higher at almost the same temperature: $T = 555$°C, $P = 6.8$ kbar. The parameters of the

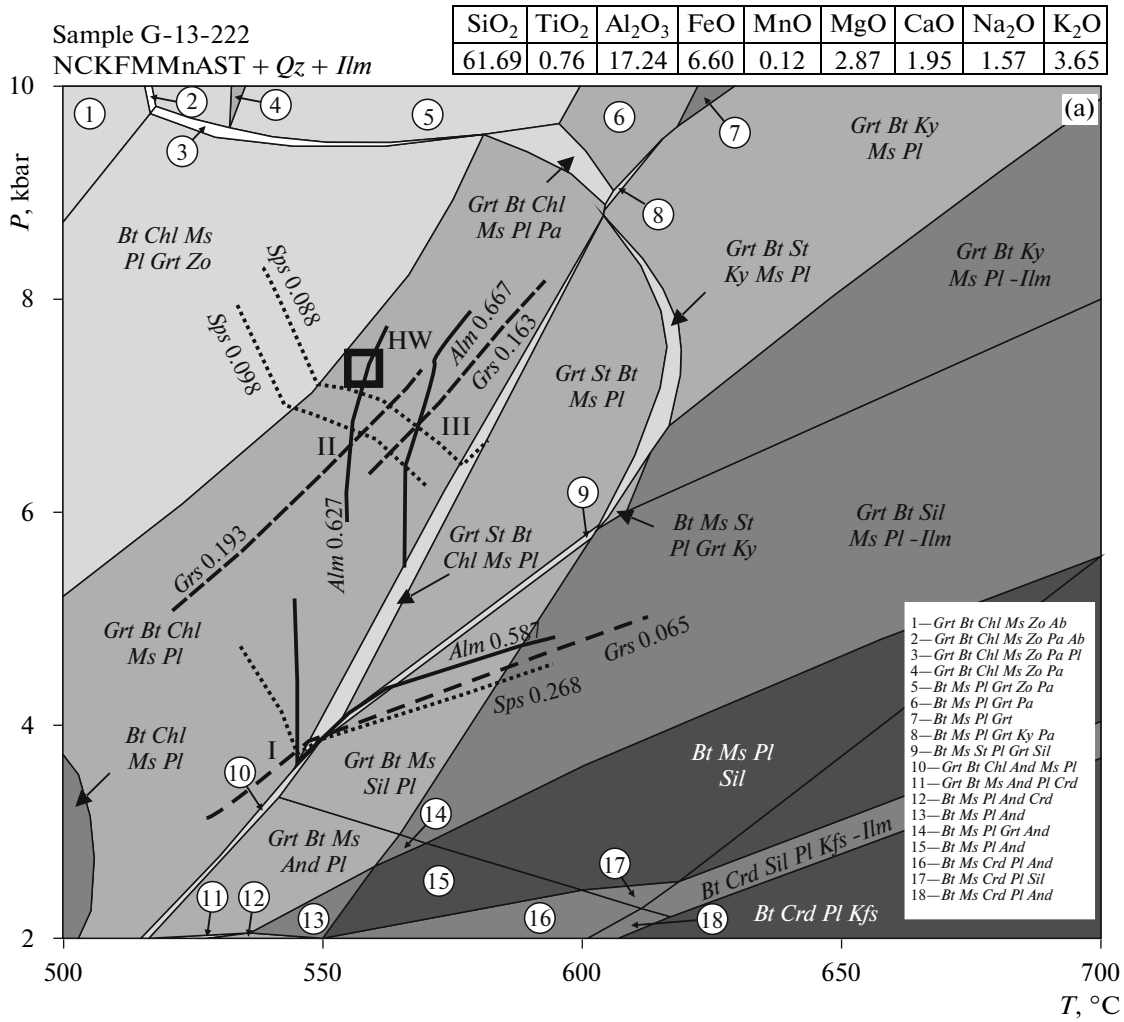

Fig. 8. Phase diagrams for samples of the aluminous schists. The diagrams show almandine, grossular, and spessartine isopleths for various zones of garnet crystals. See Table 2 for the garnet analyses; see Fig. 3 for the micrographs and concentration profiles. The square labeled HW indicates the *P–T* parameters calculated with the *Grt–Bt* geothermometer and *Grt–Bt–Pl–Qz* geobarometer (Holdaway, 2000; Wu et al., 2004). I, II, and III are the intersections of the compositional isopleths of first-, second-, and third-population garnet, respectively; IIc and IIi are the composition of the second-population garnet closer to the grain center and to its margin, respectively. Heavy solid lines are almandine isopleths, dashed lines are grossular isopleths, dotted lines are spessartine isopleths.

third (outermost) zone are $T = 565°C$, $P = 6.8$ kbar. The parameters yielded by the GB geothermometer and GBPQ geobaroimeter are $T = 559°C$ and $P = 7.3$ kbar (Table 6). The isopleths of all three generations intersect in the *Grt + Bt + Ms + Chl + Pl + Qz + Ilm* field, which is consistent with petrographic observations.

Sample G-13-200 (Fig. 8b). The *P–T* parameters calculated for the central high-Ca part correspond to $T = 530°C$, $P = 6.8$ kbar; the margins are characterized by a higher temperature at an almost the same pressure: $T = 570°C$ and $P = 7.2$ kbar. The values yielded by the geothermometers are similar: $T = 555°C$, $P = 7.6$ kbar.

Sample G-13-211 (Fig. 8c). The intersection of isopleths for the central part of the grain, which host an S-shaped trails of mineral inclusions, yields $T = 530°C$, $P = 5.7$ kbar; the intersection for the rim corresponds to $T = 560°C$, $P = 6.4$ kbar. The geothermometers yield $T = 560°C$, $P = 6.9$.

Staurolite Zone

The rocks of this zone contain all three or only the second and third generations of garnet grains. The garnet of the first generation falls into the field of the *Grt + Crd + Bt + Sil + Pl + Qz + Ilm* mineral assemblage, and the second-generation garnet plots within the *Grt + Bt + Ms + Chl + Pl + Qz + Ilm* field, as also does the garnet of the garnet zone. The garnet of the third

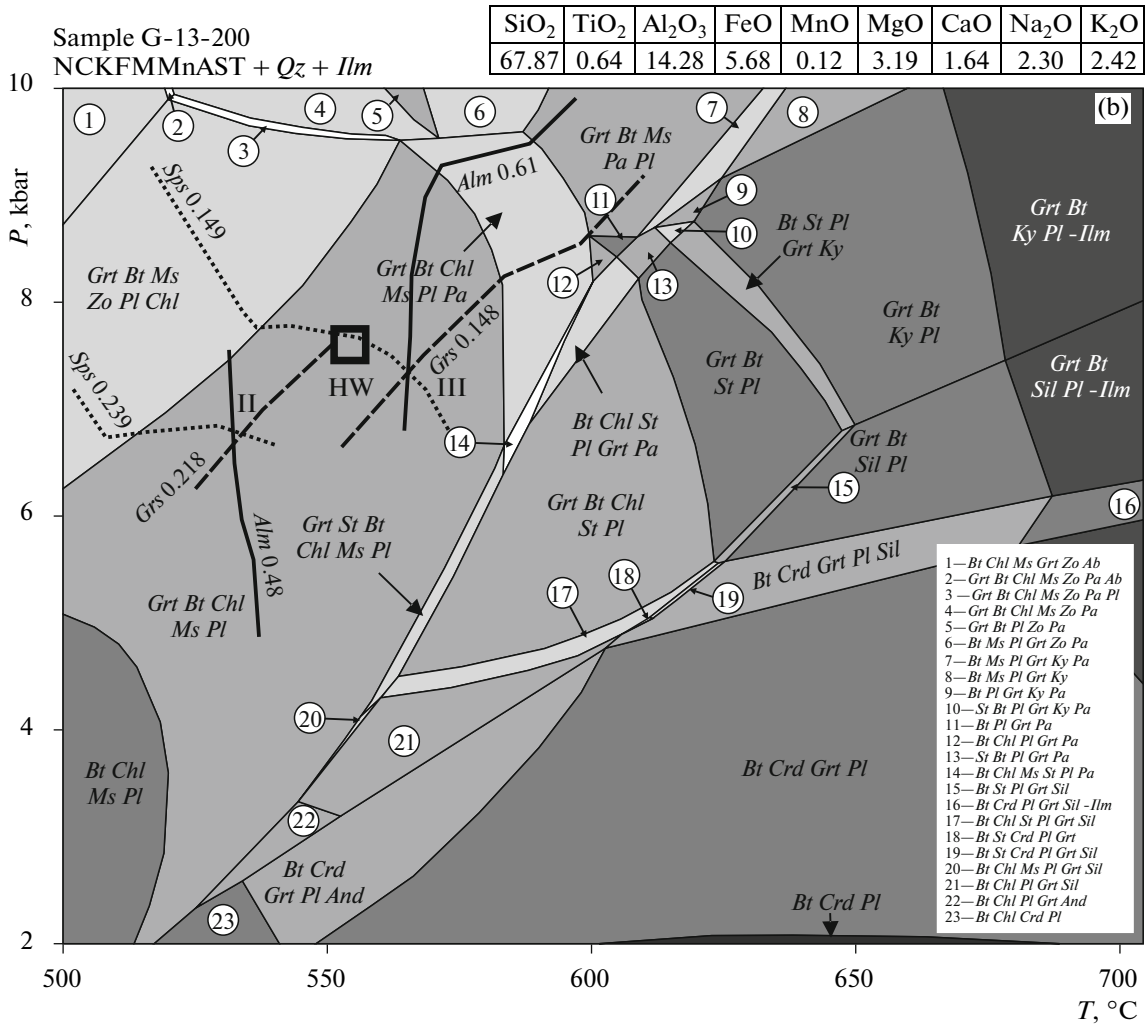

Fig. 8. (Contd.)

generation is stable within the *Grt* + *St* + *Bt* + *Ms* + *Pl* + *Pa* + *Qz* + *Ilm* (sample G13-27), *Bt* + *Chl* + *Ms* + *St* + *Pl* + *Grt* + *Qz* + *Ilm* (sample G-13-18), and *Bt* + *Ms* + *St* + *Pl* + *Grt* + *Ky* + *Qz* (sample G-13-16) fields.

Sample G-13-16 (Fig. 8d). The diagram shows isopleths for the cores, intermediate zones, and outermost rims of garnet grains; for these and other samples discussed below, we made use of pairs of analyses for their intermediate zones: one closer to the grain centers (denoted IIc) and the other with the maximum grossular concentration (IIi). The *P–T* parameters of the cores are $T = 570°C$, $P = 3.3$ kbar; and those of the intermediate zone $T = 560°C$, $P = 6$ kbar (IIc) and $T = 575°C$, $P = 7.8$ kbar (IIi). The outer rim yields $T = 605–615°C$, $P = 7–7.8$ kbar. The diagram also shows isopleths of the composition of the hopper garnet crystals (samples G-13-16a, b, c), which turned out to be closely similar to the outer garnet rims: $T = 615–620°C$, $P = 7–7.2$ kbar. The values yielded by the geothermometer and geobarometer (GB and GBPQ) lie between the values for the intermediate zones and outermost rims: $T = 600°C$, $P = 7.5$ kbar.

Sample G-13-18 (Fig. 8e). The core yielded $T = 575°C$, $P = 3.1$ kbar; and the intermediate zone (IIc) gave $T = 530°C$, $P = 5.2$ kbar (IIi) and $T = 565°C$, $P = 5.2$ kbar (IIi). The outermost rim was formed under a higher pressure: $T = 575°C$, $P = 7.8$ kbar.

Sample G-13-37 (Fig. 8f). Garnet in this sample has got no core of the first generation. The diagram shows the composition of the central part (IIc), intermediate zone with the highest grossular concentration (IIi), and the outermost rim. The high-Ca zone was formed under a higher pressure of $P = 6.8$ kbar than the core, $P = 5.5$ kbar; the temperature varied insignificantly: $T = 520–540°C$. The temperature for the outermost zone is higher at a slightly higher pressure: $T = 590°C$, $P = 7.1$ kbar.

The overall evolutionary *P–T* path of metamorphism of the aluminous schists is displayed in Fig. 9.

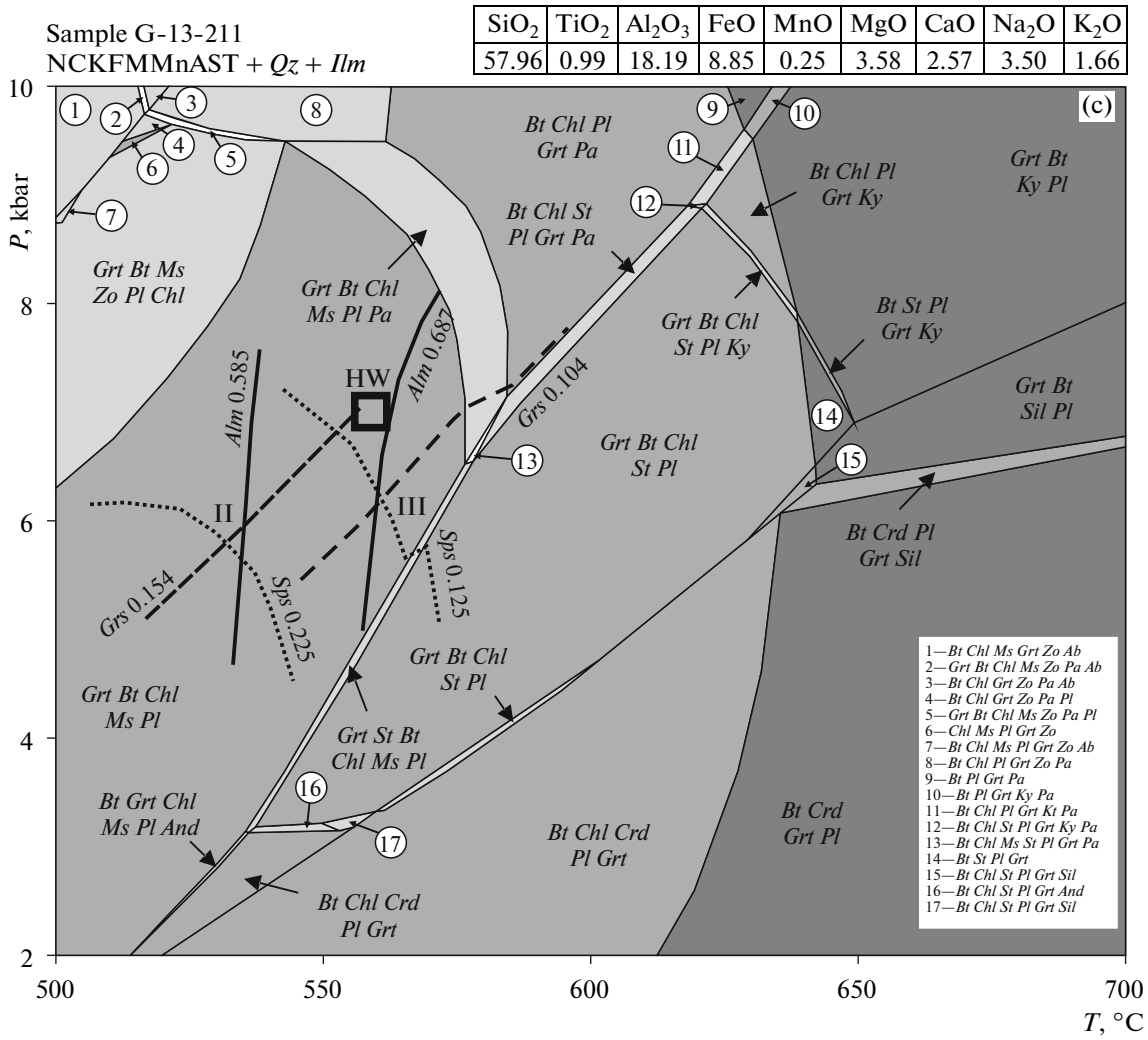

Fig. 8. (Contd.)

TEMPERATURE GRADIENTS ESTIMATED BY MODEL GEOTHERMS

The probable source of heat for collisional orogens can be (1) mafic magmas, (2) elevated contents of radioactive heat sources in the thickened granitic crust; and (3) heat sources related to viscous friction in local shear zones (Burg and Gerya, 2005; Schmalholz and Podladchikov, 2013). All of the aforementioned types of heat sources could contribute to the temperature increase during the first (high-gradient) metamorphic episode. Evidence of the first of the heat sources is provided by mafic dikes, which were emplaced before the low-gradient metamorphic episode (Kozakov, 1986). The second (radiogenic) heat source is quite probable with regard for the significant crustal thickness beneath the Mongolian Altai and for the high content of granitic material in this crust. Elevated heat production was earlier detected in the Bogodchin granite massif of the complex: 1.66 μW/m^3 as compared with the crustal average value of 0.7–0.9 μW/m^3 (Polyansky et al., 2011). Finally, the third type of heat sources (viscous–dissipative) is also probable in view of the great number of deformation zones composed of cataclasite, mylonite, and blastomylonite. Elucidation of heat source during the high-gradient metamorphic episode is beyond the scope of this publication. A 2D thermal–tectonic model for the collisional evolutionary episode of the Tsel metamorphic block of the Mongolia Altai is suggested in (Polyansky et al., 2015), and here we limit ourselves to merely approximate estimates obtained by solving a steady-state thermal conductivity equation for various thermal regimes of the continental crust, as was previously done in (Spear, 1993).

Steady-state geotherms were calculated using a thermal conductivity equation at an even distribution of radioactive heat sources over a single-layer crust (Spear, 1993):

$$T = T_{\text{surf}} + \left(\frac{Q}{k} + \frac{AD}{k}\right)z - \frac{A}{2k}z^2,$$

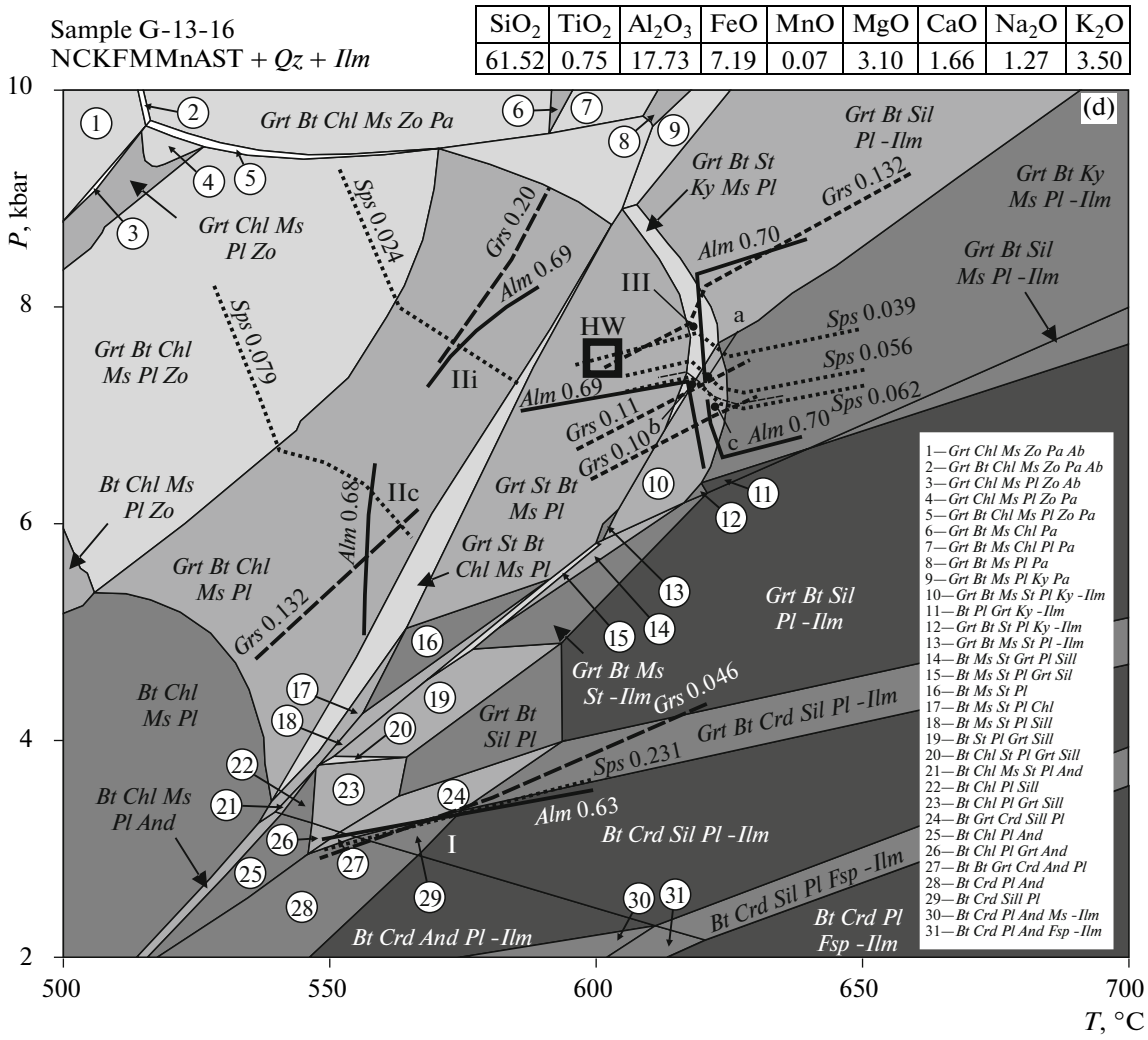

Fig. 8. (Contd.)

where T_{surf} (°C) is the temperature at the surface, k (W/m K) is the thermal conductivity, Q (mW/m^2) is the mantle heat flow, A (μW/m^3) is the radioactive heat production, D (m) is the thickness of the crust (radiogenic layer), and z (m) is the depth beneath the surface. Parameters of the curves are listed in Table 7. In constructing the geotherms, we assumed that (1) the thickened crust has a granitic layer that is of elevated thickness and is enriched in radioactive heat sources; (2) the high-gradient region is characterized by a twice higher heat flow than the crustal average values, and the protolith of the metapelites is characterized by lower heat conductivity, as is typical of dry terrigenous sediments. Figure 9 displays geotherms typical of various tectonic environments: average continental crust, thickened continental crust, and a heated high-gradient crustal region. The latter two variants correspond to the *P–T* parameters of the two metamorphic episodes estimated by geothermobarometers.

DISCUSSION

Our data indicate that the first garnet generation (grain cores) was formed at T = 570–575°C in the staurolite zone and at 545°C in the garnet zone; the pressure was P = 3.1–3.7 kbar (Table 6), which corresponds to an elevated thermal gradient of 40–50°C/km.

The garnet of the second generation is much richer in grossular than the first-generation garnet. Thermobarometric calculations indicate that the second-generation garnet grew at a pressure increase and a merely insignificant temperature increase. The maximum pressure values are yielded by garnet compositions richest in Ca and are 5.7–6.8 kbar for the garnet zone and 6.8–8 kbar for the staurolite zone.

The garnet of the third generation grew at a higher temperature than that of the second-generation garnet, while the pressure has not practically changed, which is consistent with the decrease in the Fe# of the garnet of the third generation. The maximum temper-

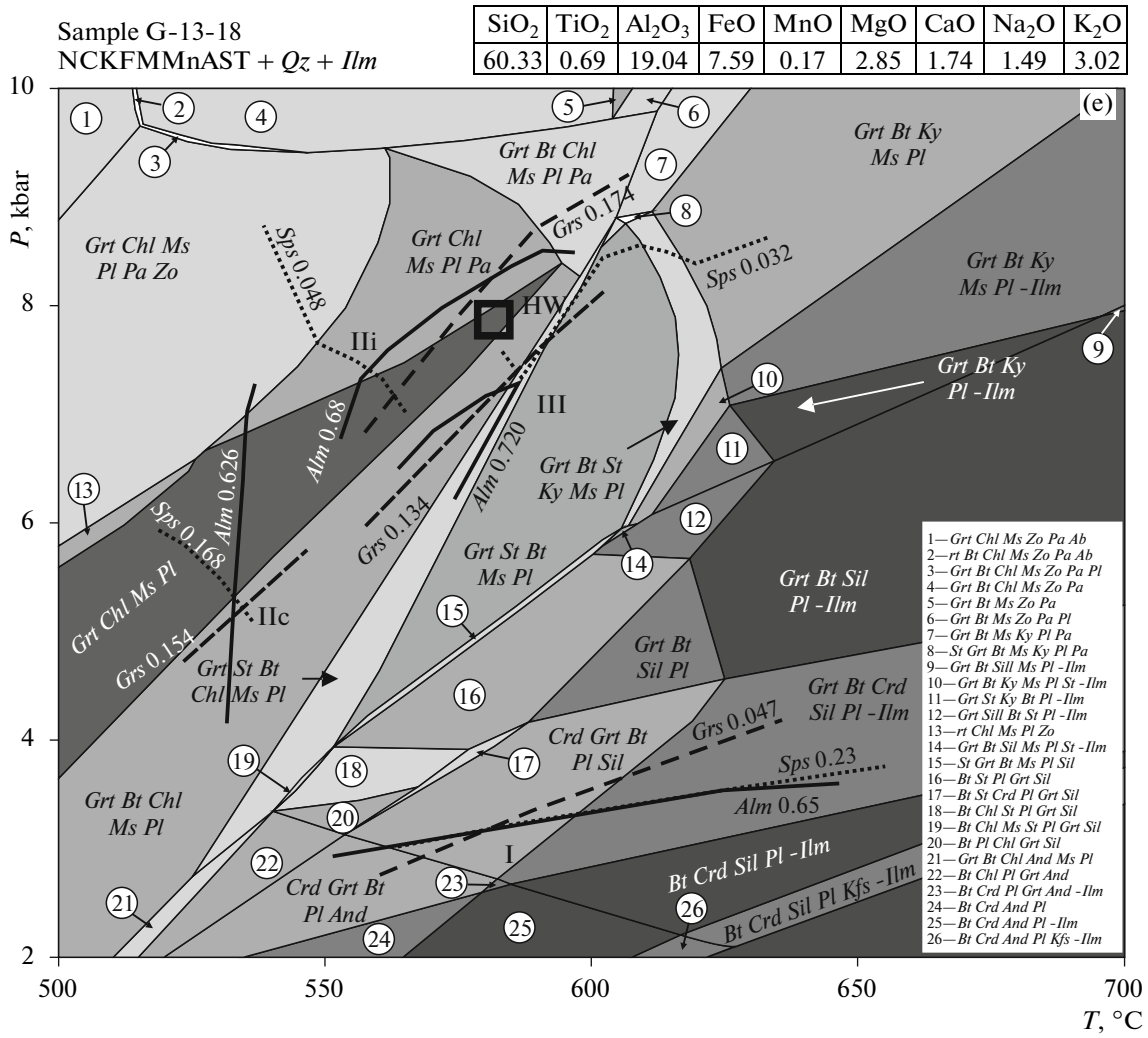

Fig. 8. (Contd.)

atures are 560–565°C for garnet in the garnet zone and 585–615°C for the mineral in the staurolite zone. Hopper garnet crystals in sample G-13-16 (G-13-16a, b, c in Table 6) were formed at the same *P–T* parameters as the outermost zones of the large garnet crystals.

Note that the composition of the second-generation garnet plots within the stability field of the *Grt* + *Bt* + *Ms* + *Chl* + *Pl* + *Qz* assemblage, and only the composition of the third-generation garnet falls into the staurolite stability field. This led us to conclude that staurolite started to grow in the rocks simultaneously with the development of the third-generation garnet rims, during the postkinematic episode. This conclusion is consistent with that mineral inclusions in the garnet grains from S-shaped trails, while inclusion trails in the staurolite grains are linear (sample G-13-27, Fig. 2a). Although mineral inclusions define linear trails in the staurolite grains, the orientation of these trails does not coincide with the foliation, which may suggest that deformations continued when the staurolite grains stopped to grow, but the deformations occurred at lower temperatures. This follows from the occurrence of muscovite in pressure shadows near staurolite grains. These deformations may have been related to the exhumation of the metamorphic blocks.

The temperature and pressure values estimated by mineralogical geothermometers and geobarometers are closely similar and often coincide within the errors (T ±50°C, P ±1 kbar) with the estimates derived from intersections of compositional isopleths for the rims of garnet grains. The differences may be explained by that different thermodynamic data on mineral end members were employed in these approaches.

The geothermal gradient at which the second- and third-generation garnet was formed was some 27°C/km, which corresponds to values calculated for the thickened crust model (Table 7, variant 2). The S-shaped inclusion trails in the second-generation garnet (which possesses elevated grossular concentrations) suggest that the garnet grew simultaneously with the deformations of the rocks. The pressure increase

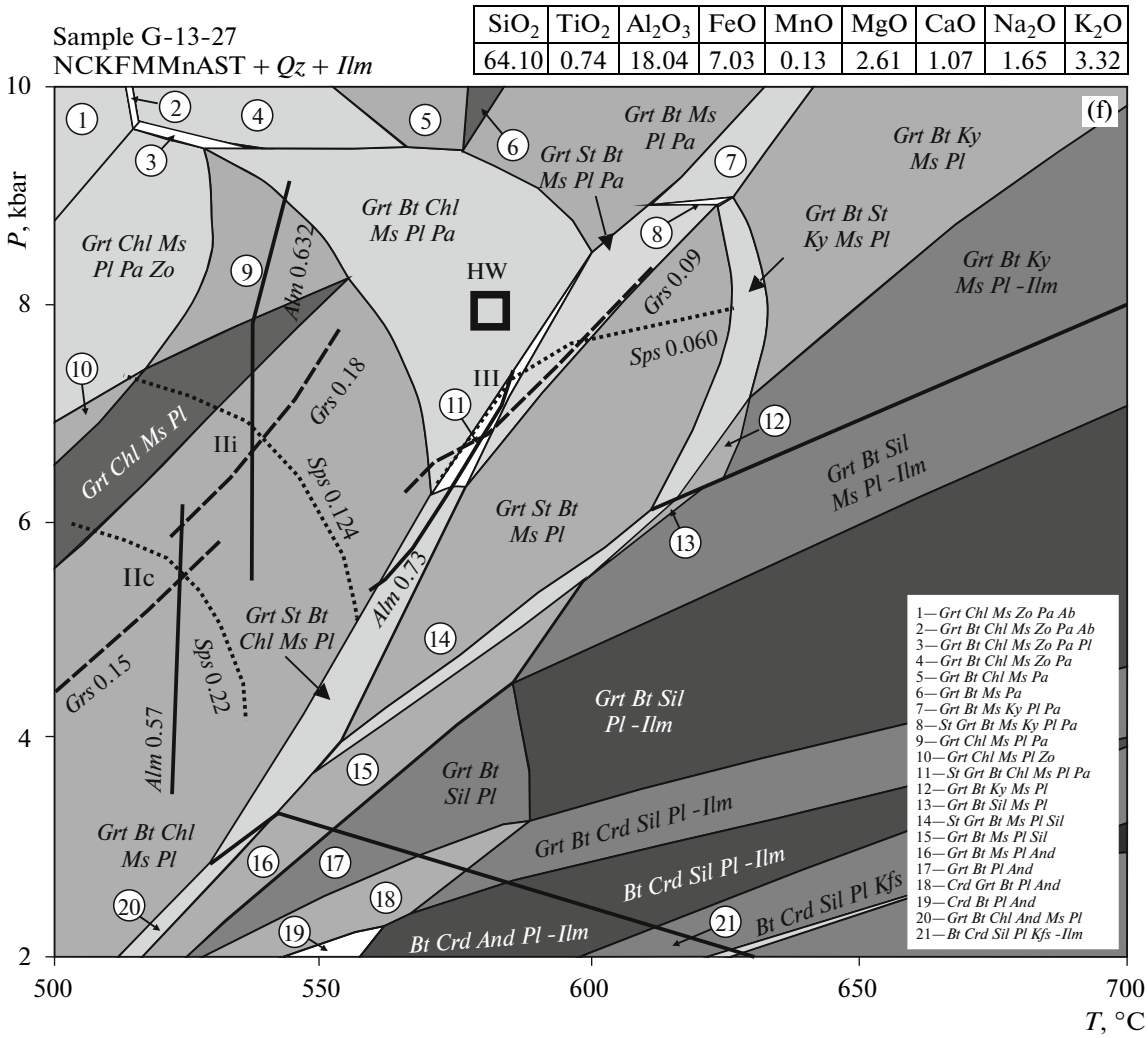

Fig. 8. (Contd.)

coeval with deformations may be explained by crustal thickening due to tectonic plate overthrusting. The configuration of the calculated *P–T* path suggests that the rocks were hosted in the footwall of the thrust. The pressure difference between the growth of the first-generation garnet and the maximum values, which were calculated for the second-generation garnet, is approximately 4–5 kbar, which corresponds to crustal thickening by 15–18 km at an average density of the continental crust of 2.7 g/cm^3.

The *P–T* paths calculated for the compositions of the second- and third-generation garnet are in good agreement with the model *P–T* paths of overthrusting regions without additional heat influx (England and Thomson, 1984; Spear, 1993). The early evolution is marked by a pressure increase at a practically unchanging temperature because of slab descent induced by the overthrusting of neighboring rocks. The direction of the *P–T* path has been eventually changed due to a temperature increase and an almost constant pressure because of sluggish heat transfer at the flattening of the geotherms.

A sequence of the metamorphic events, with the transition from high- to low-gradient metamorphism, analogous to that suggested for our rocks was previously reproduced for the Southern Altai Metamorphic Belt in (Kozakov, 1986; and others) with regard for data of folding analysis. An analogous conclusion was derived from kyanite pseudomorphs after andalusite found in the Tseel-somon area (Sukhorukov, 2007).

Current tectonic models for the Southern Mongolian Metamorphic Belt suggest that it was produced during two metamorphic episodes. The older one occurred at an elevated temperature gradient and resulted in granulite-facies rocks (in the Tsogt block) and rocks of lower grades (in the Bogodchin and Tseel blocks). This episode was dated at 380–390 Ma. The second episode was of the kyanite–sillimanite type, and its parameters reached the epidote-amphibolite and amphibolite metamorphic facies. The mineral

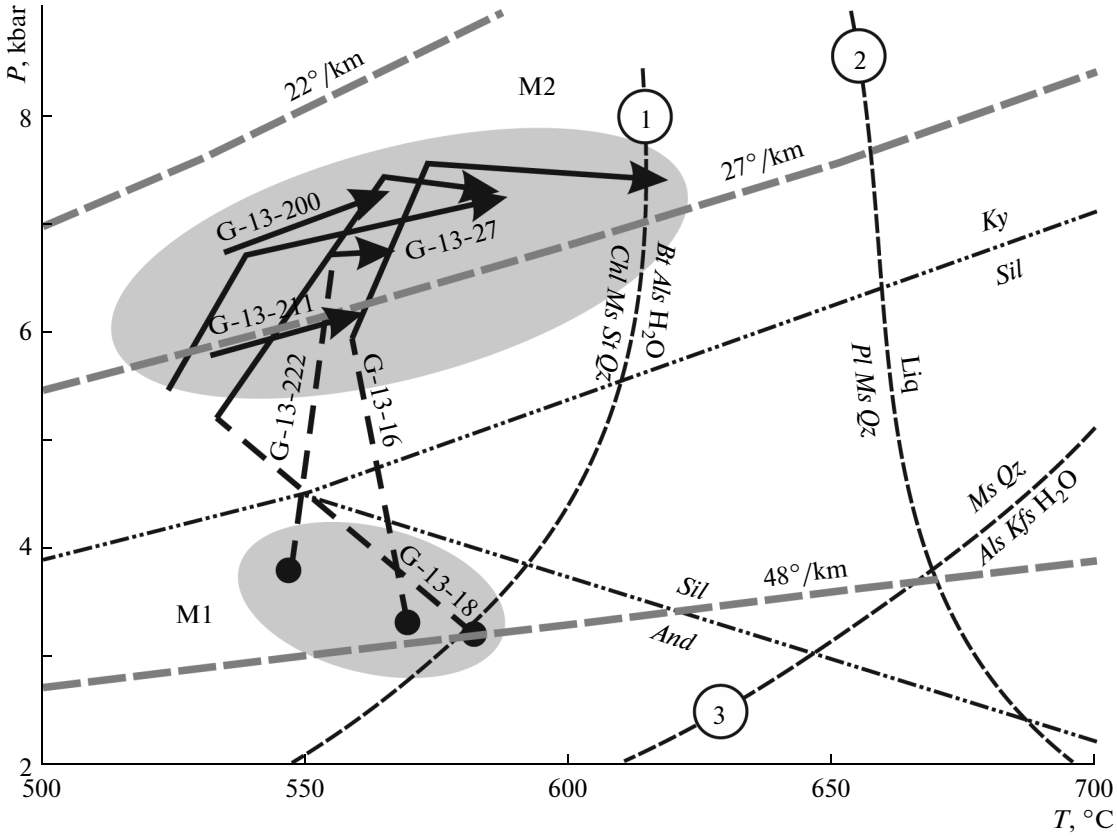

Fig. 9. Integral $P–T$ metamorphic path of the aluminous schists inferred from geothermobarometric data (Fig. 8). M1 is the old high-gradient metamorphism, M2 is the medium-temperature, medium-pressure metamorphism. Numerals indicate mineral equilibria for the metapelite system: (1) (Pattison, 2001), (2) (Chatterjee and Johannes, 1974), (3) is the pelite solidus in a water-saturated system (Le Breton and Thompson, 1988). The triple point of Al_2SiO_5 polymorphs is according to (Pattison, 1992). Geotherms are plotted according to data in Table 7.

assemblages of the second episode are in places replaced on the assemblages of the first episode, while the latter has not left any traces elsewhere, and other rocks display traces only of the second metamorphic episode. The age of the kyanite–sillimanite metamorphism was estimated in the synmetamorphic intrusions at 370–360 Ma (Bibikova et al., 1992). Events of this age also left traces on the continuation of the Southern Mongolian Belt in the Chinese Altai and Irtysh Shear Zone in eastern Kazakhstan. The tectonic models are published in (Mossakovskii et al., 1993; Didenko et al., 1994; Ruzhentsev and Pospelov, 1992; Kozakov et al., 2011; and others). The Southern Altai belt had thus been formed by 360 Ma, but deformations and granite magmatism continued in Permian time (Kozakov et al., 2011), as follows from numerous $^{39}Ar/^{40}Ar$ dates of amphibole and micas from metamorphic schists sampled in the Southern Altai Belt. All of these dates fall within the range of 275–250 Ma (Polyansky et al., 2011).

Younger dates of metamorphic rocks were occasionally obtained in both the Southern Altai Metamorphic Belt itself and its continuation in the Chinese Altai. Massive monazite dating with correlations with mineral assemblages led the authors of (Nakano et al., 2014, 2015) to distinguish two metamorphic events in aluminous schists from the Bodonchin block in the western part of the Tseel Metamorphic Belt. The older event was high-gradient metamorphism at 360 Ma, and the younger one is thought to be related to a pressure increase and is characterized by an intermediate geothermal gradient of 25°C/km; this event was dated at approximately 277 Ma. The second metamorphic event was reportedly related to a collisional environment during the closure of the Paleo-Asian Ocean.

The latest structural–geochronologic studies in the Irtysh Zone and the Chinese Altai on the continuation of the Bulgan fault have shown that major regional collisional events took place between 322 Ma (the age of the youngest detrital zircon in the schists) and 252 Ma (the age of the cutting granite dikes) (Li et al., 2015). These events are thought to have been related to collision between the Chinese Altai and western Dzhungaria.

In the absence of dates on the schists, it is impossible to reliably date this metamorphic event, but similarities between the $P–T$ parameters and geothermal gradient (approximately 25°/km) suggest that this

Table 6. *P-T* metamorphic parameters of the aluminous schists

	Sample	Population						H2000	WU2004
		I		II		III			
		T, °C	*P*, kbar	*T*, °C	*P*, kbar	*T*, °C	*P*, kbar	*T*, °C	*P*, kbar
Garnet zone	G-13-222	545	3.7	555	6.8	565	6.8	559	7.3
	G-13-200			525	6.8	565	7.2	555	7.6
	G-13-211			530	5.7	560	6.4	560	6.9
Staurolite zone	G-13-16	570	3.3			605–615	7–7.8	600	7.5
	IIc			560	6				
	IIi			575	7.8				
	a, b, c					615–620	7–7.2		
	G-13-18	575	3.1			585	7.3	575	7.8
	IIc			530	5.2				
	IIi			565	7–8				
	G-13-27								
	IIc			520	5.5	590	7.1	575	7.7
	IIi			540	6.8				

Estimates of the *P-T* metamorphic parameters for various garnet populations (I, II, and III) were obtained from intersections of compositional isopleths, H2000 and WU2004 are estimates by the geothermometer (Holdaway, 2000) and geobarometer (Wu et al., 2004) for the marginal parts of garnet grains and matrix minerals.

Table 7. Parameters for calculation of the geothermal curves

Variant	*K*, W/m K	*A*, μW/m^3	*Q*, mW/m^2	*D*, km
1	2.25	0.95	17	40
2	2.25	0.95	17	50
3	1.4	0.95	35	40

Variant 1 is an average continental crust, variant 2 is a thickened crust, and variant 3 is a crust with an elevated heat flux. The parameters are assumed according to (Spear, 1993; Hacker et al., 2011).

metamorphic event was likely coeval with the kyanite–sillimanite metamorphism distinguished in (Kozakov, 1986; and others). It is reasonable to suggest that the oldest (high-gradient) metamorphic episode belonged to another individual metamorphic cycle or could be the starting episode of the low-gradient metamorphism and can be combined with the latter within a single cycle. The absence of any traces of retrogression after the origin of the garnet cores and the absence of zoning in the distribution of mineral assemblages of the oldest metamorphic episode can be explained by crustal thickening at the transition to the collisional tectonic environment.

CONCLUSIONS

(1) Garnet and staurolite schists in the Gegetin-Gol area contain three garnet generations. The garnet of the first generation occurs as grain cores and possesses the lowest grossular concentrations and high almandine and spessartine concentrations. The second generation bears quartz and ilmenite inclusions and is rich in grossular. The garnet of the third generation develops as the outermost rims and hopper crystals and contains less grossular than the second-population garnet. The garnet of the second generation grew simultaneously with deformations of the rocks,

as follows from S-shaped trails of mineral inclusions in its grains.

(2) Aluminous schists in the Gegetin-Gol area were affected by metamorphism of two successive episodes: high-gradient metamorphism of the andalusite–sillimanite type, geothermal gradient approximately 40–50°C/km and low-gradient metamorphism of the kyanite–sillimanite type, geothermal gradient approximately 27°C/km. The $P–T$ parameters of the older episode were $T = 545–575$°C, $P = 3.1–3.7$ kbar. The younger episode was characterized by zonal metamorphism, whose peak parameters were $T = 560–565$°C, $P = 6.4–7.2$ for the garnet zone and $T = 585–615$°C, $P = 7.1–7.8$ for the staurolite zone.

(3) The $P–T$ metamorphic evolution of the area is described by a clockwise $P–T$ path: a pressure increase at a practically unchanging temperature during the first episode and a temperature increase at a practically constant pressure during the second one. This trend is consistent with models for thrusting terranes without additional heat sources. The crustal thickening was at least 15–18 km.

ACKNOWLEDGMENTS

The authors thank A.B. Kotov and I.K. Kozakov (Institute of Precambrian Geology and Geochronology, Russian Academy of Sciences); and L.Ya. Aranovich and S.P. Korikovsky (Institute of the Geology of Ore Deposits, Petrography, Mineralogy, and Geochemistry, Russian Academy of Sciences) for valuable comments that helped us to improve the content of the manuscript. This study was financially supported by the Russian Foundation for Basic Research (project nos. 15-05-00598, 14-05-00188, 14-05-00117) and a project under the Earth Science Department of the Russian Academy of Sciences.

REFERENCES

Aranovich, L.Ya., *Mineral'nye ravnovesiya mnogokomponentnykh tverdykh rastvorov* (Mineral Equilibria of Multicomponent Solid Solutions), Moscow: Nauka, 1991.

Ayres, M. and Vance, D., A comparative study of diffusion profiles in Himalayan and Dalradian garnets: constraints on diffusion data and the relative duration of the metamorphic events, *Contrib. Mineral. Petrol.,* 1997, vol. 128, pp. 66–80.

Badarch, G., Cunningham, W.D., and Windley, B.F., A new terrane subdivision for Mongolia: implications for Phanerozoic crustal growth of central Asia, *J. Asian Earth Sci.,* 2002, vol. 21, pp. 87–110.

Bibikova, E.V., Kirnozova, T.I., Kozakov, I.K., et al., Polymetamorphic complexes of the southern slope of Mongolian Altai: results of U-Pb dating, *Geotektonika,* 1992, no. 2, pp. 104–112.

Burenjargal, U., Okamoto, A., and Meguro, Y., An exhumation pressure–temperature path and fluid activities during metamorphism in the Tseel terrane, SW Mongolia: constraints from aluminosilicate-bearing quartz veins and garnet zonings in metapelites, *J. Asian Earth Sci.,* 2012, vol. 54–55, pp. 214–229.

Burenjargal, U., Okamoto, A., Kuwatani, T., et al., Thermal evolution of the Tseel terrane, SW Mongolia and its relation to granitoid intrusions in the central Asian Orogenic Belt, *J. Metamorph. Geol.,* 2014, vol. 32, pp. 765–790.

Burg, J.-P. and Gerya, T., The role of viscous heating in Barrovian metamorphism of collisional orogens: thermomechanical models and application to the Lepontine Dome in the central Alps, *J. Metamorph. Geol.,* 2005, vol. 23, pp. 75–95.

Caddick, M., Konopasek, J., and Thompson, A.B., Preservation of garnet growth zoning and the duration of prograde metamorphism, *J. Petrol.,* 2010, vol. 51, pp. 2327–2347.

Caddick, M.J. and Kohn, M.J., Garnet: witness to the evolution of destructive plate boundaries, *Elements,* 2013, vol. 9, pp. 427–432.

Carlson, W.D., The significance of intergranular diffusion to the mechanism and kinetics of porphyroblast crystallization, *Contrib. Mineral. Petrol.,* 1989, vol. 103, pp. 1–24.

Carlson, W.D., Scales of disequilibrium and rates of equilibrium during metamorphism, *Am. Mineral.,* 2001, vol. 87, pp. 185–200.

Chakraborty, S. and Ganguly, J., Cation diffusion in aluminosilicate garnets: experimental determination in spessartine–almandine diffusion couples, evaluation of effective binary, diffusion coefficients, and applications, *Contrib. Mineral. Petrol.,* 1992, vol. 111, pp. 74–86.

Chatterjee, N.D. and Johannes, W.S., Thermal stability and standard thermodynamic properties of synthetic $2M_1$-muscovite, $KAl_2Al_3Si_3O_{10}(OH)_2$, *Contrib. Mineral. Petrol.,* 1974, vol. 48, pp. 89–114.

Connolly, J.A.D., Multivariable phase diagrams: an algorithm based on generalized thermodynamics, *Am. J. Sci.,* 1990, vol. 290, pp. 666–718.

Connolly, J.A.D., The geodynamic equation of state: what and how, *Geochem., Geophys., Geosyst.,* 2009, vol. 10, p. 10.

Didenko, A.N., Mossakovskii, A.A., Pecherskii, D.M., et al., Geodynamics of the Paleozoic oceans in Central Asia, *Geol. Geofiz.,* 1994, vol. 35, nos. 7–8, pp. 59–75.

Dohmen, R. and Chakraborty, S., Mechanism and kinetics of element and isotopic exchange mediated by a fluid phase, *Am. Mineral.,* 2003, vol. 88, pp. 1251–1270.

England, P.C. and Thompson, A.B., Pressure temperature time paths of regional metamorphism 1. Heat transfer during the evolution of regions of thickened continental crust, *J. Petrol.,* 1984, vol. 25, pp. 894–928.

Evans, T.P., A method for calculating effective bulk composition modification due to crystal fractionation in garnet-bearing schist: implications for isopleth thermobarometry, *J. Metamorph. Geol.,* 2004, vol. 22, pp. 547–557.

Florence, F.P. and Spear, F.S., Effects of diffusional modification of garnet growth zoning on $P–t$ path calculations, *Contrib. Mineral. Petrol.,* 1991, vol. 107, pp. 487–500.

Gerya, T.V., Perchuk, L.L., van Reenen, D.D., and Smit, C.A., Two-dimensional numerical modeling of pressure–temperature–time paths for the exhumation of some granulite facies terrains in the Precambrian, *J. Geodynam.,* 2000, vol. 29, pp. 17–35.

Herron, M.M., Geochemical classification of terrigenous sands and shales from core or log date, *J. Sed. Petrol.,* 1988, vol. 58, pp. 820–829.

Holdaway, M.J., Application of new experimental and garnet Margules data to the garnet–biotite geothermometer, Am. Mineral., 2000, vol. 85, pp. 881–889.

Holland, T.J.B. and Powell, R., An internally consistent thermodynamic data set for phases of petrological interest, *J. Metamorph. Geol.,* 1998, vol. 16, pp. 309–343.

Jamieson, R.A., Beaumont, C., Nguyen, M.H., and Lee, B., Interaction of metamorphism, deformation, and exhumation in large convergent orogens, *J. Metamorph. Geol.,* 2002, vol. 20, pp. 9–24.

Jiang, Y., Sun, M., Kröner, A., et al., The high-grade Tseel terrane in SW Mongolia: an Early Paleozoic arc system or a Precambrian sliver?, *Lithos,* 2012, vol. 142–143, pp. 95–115.

Kim, H.S. and Bell, T.H., Combining compositional zoning and foliation intersection axes (FIAs) in garnet to quantitatively determine early *P–T–t* paths in multiply deformed and metamorphosed schists: north central Massachusetts, USA, *Contrib. Mineral. Petrol.,* 2005, vol. 149, pp. 141–163.

Kohn, M.J., Geochemical zoning in metamorphic minerals, in *Treatise on Geochemistry. Vol. 3. The Crust,* Rudnick, R., Ed., Oxford: Elsevier–Pergamon, 2005, vol. 3, pp. 229–261.

Kozakov, I.K., *Dokembriiskie infrastrukturnye kompleksy Mongolii* (Precambrian Infrastructural Complexes in Mongolia), Leningrad: Nauka, 1986.

Kozakov, I.K., Kovach, V.P., Bibikova, E.V., et al., Age and sources of granitoids in the junction zone of the Caledonides and Hercynides in southwestern Mongolia: geodynamic implications, *Petrology,* 2007, vol. 15, no. 2, pp. 126–150.

Kozakov, I.K., Didienko, A.N., Azimov, P.Ya., et al., Geodynamic settings and formation conditions of crystalline complexes in the South Altai and South Gobi metamorphic belts, *Geotectonics,* 2011, vol. 45, no. 3, pp. 174–194.

Kröner, A., Windley, B.F., Badarch, G., et al., Accretionary growth and crust formation in the Central Asian Orogenic Belt and comparison with the Arabian–Nubian shield, in *4-D Framework of Continental Crust,* Hatcher, R.D., Jr., Carlson, M.P., McBride, J.H., Martínez Cátalan J.R., Eds., *Geol. Soc. Am. Mem.* 2007, vol. 200, pp. 181–209.

Le Breton, N. and Thompson, A.B., Fluid-absent (dehydration) melting of biotite in metapelites in the early stages of crustal anatexis, *Contrib. Mineral. Petrol.,* 1988, vol. 99, pp. 226–237.

Li, P., Sun, M., Rosenbaum, G., et al., Structural evolution of the Irtysh shear zone (northwestern China) and implications for the amalgamation of arc systems in the Central Asian Orogenic Belt, *J. Struct. Geol.,* 2015. doi 10.1016/j.jsg.2015.08.008

Likhanov, I.I., Reverdatto, V.V., Kozlov, P.S., et al., Three metamorphic events in the Precambrian *P–T–t* history of the Transangarian Yenisey Ridge recorded in garnet grains in metapelites, *Petrology,* 2013, vol. 21, no. 6, pp. 561–578.

Menard, T. and Spear, F.S., Metamorphism of calcic pelitic schists, Strafford Dome, Vermont: compositional zoning and reaction history, *J. Petrol.,* 1993, vol. 34, pp. 977–1005.

Mossakovskii, A.A., Ruzhentsev, S.V., Samygin, S.G., and Kheraskova, T.N., Central Asian Fold Belt: geodynamic evolution and history of formation, *Geotektonika,* 1993, no. 6, pp. 3–32.

Nakano, N., Osanai, Y., Satish-Kumar, M., et al., Paleozoic subduction–accretion–closure histories in the West Mongolian segment of the Paleo-Asian ocean: evidence from pressure–temperature–time–protolith evolution of high-Mg and -Al gneisses in the Altai mountains, *J. Geol.,* 2014, vol. 122, pp. 283–308.

Nakano, N., Osanai, Y., Owada, M., et al., Multiple growth of garnet, sillimanite/kyanite and monazite during amphibolite facies metamorphism: implications for the *P–T–t* and tectonic evolution of the western Altai Range, Mongolia, *J. Metamorph. Geol.,* 2015, vol. 33, no. 9, pp. 909–1046.

Newton, R.C., Charlu, T.V., and Kleppa, O.J., Thermochemistry of the high structural state plagioclases, *Geochim. Cosmochim. Acta,* 1980, vol. 44, pp. 933–941.

Pattison, D.R.M., Stability of andalusite and sillimanite and the Al_2SiO_5 triple point: constraints from the Ballachulish aureole, *Scot. J. Geol.,* 1992, vol. 100, pp. 423–446.

Pattison, D.R.M., Instability of Al_2SiO_5 "triple point" assemblages in muscovite + biotite + quartz-bearing metapelites, with implications, *Am. Mineral.,* 2001, vol. 86, pp. 1414–1422.

Perchuk, L.L., Aranovich, L.Ya., Podlesskii, K.K., et al., Precambrian granulites of the Aldan Shield, eastern Siberia, USSR, *J. Metamorph. Geol.,* 1985, vol. 3, pp. 265–310.

Polyansky, O.P., Sukhorukov, V.P., Travin, A.V., et al., Tectonic interpretation of the thermochronological data and *P-T* conditions of rock metamorphism in the Bodonchin Zone complex (Mongolian Altai), *Russ. Geol. Geophys.,* 2011, vol. 52, no. 9, pp. 991–1006.

Polyansky, O.P., Babichev, A.V., Sukhorukov, V.P., et al., A thermotectonic numerical model of collisional metamorphism in the Mongolian Altai, *Dokl. Earth Sci.,* 2015, vol. 465, no. 2, pp. 1–5.

Ruzhentsev, S.V. and Pospelov, I.I., South-Mongolian Variscan fold system, *Geotektonika,* 1992, no. 5, pp. 45–62.

Schmalholz, S.M. and Podladchikov, Y.Y., Tectonic overpressure in weak crustal–scale shear zones and implications for the exhumation of high-pressure rocks, *Geophys. Res. Lett.,* 2013, vol. 40, pp. 1984–1988. doi 10.1002/grl.50417

Selverstone, J., Petrological constraints on imbrication, metamorphism and uplift in the SW Tauern Window, Eastern Alps, *Tectonics,* 1985, vol. 4, pp. 687–704.

Sengör, A.M.C., Natal'in, B.A., and Burtman, V.S., Evolution of the Altaid tectonic collage and Paleozoic crustal grows in Eurasia, *Nature,* 1993, vol. 34, no. 6435, pp. 299–307.

Spear, F.S., *Metamorphic Phase Equilibria and Pressure–Temperature–Time Paths,* Mineral. Soc. Am. Monogr, Washington: Book Crafters, 1993.

Stowell, H.H., Taylor, D.L., Tinkham, D.L., et al., Contact metamorphic *P–T–t* paths from Sm–Nd garnet ages, phase equilibria modelling and thermobarometry: garnet

ledge, south-eastern Alaska, USA, *J. Metamorph. Geol.,* 2001, vol. 19, pp. 645–660.

Sukhorukov, V.P., Composition and conditions of formation of andalusite–kyanite–sillimanite pegmatoid segregations in metamorphic rocks of the Tsel Block, Mongolian Altay, *Russ. Geol. Geophys.,* 2007, vol. 48, no. 6, pp. 617–622.

Tajcmanova, L., Connolly, J.A.D., and Cesare, B., Thermodynamic model for titanium and ferric iron solution in biotite, *J. Metamorph. Geol.,* 2009, vol. 27, pp. 153–165.

Tomurtogoo, O., A new tectonic scheme of the Paleozoic in Mongolia, *Mongol. Geoscient.,* 1997, vol. 3, pp. 12–17.

Warren, C.J., Beaumont, C., and Jamieson, R.A., Modelling tectonic styles and ultra-high pressure (UHP) rock exhumation during the transition from oceanic subduction to continental collision, *Earth Planet. Sci. Lett.,* 2008, vol. 267, pp. 129–145.

Werner, C.D., Saxonian granulites—a contribution to the geochemical diagnosis of original rocks in high-metamorphic complexes, *Cerlands Beitr. Geophys.,* 1987, vol. 96, pp. 271–290.

Windley, B.F., Alexeiev, D., Xiao, W.J., et al., Tectonic models for accretion of the Central Asian Orogenic Belt, *J. Geol. Soc.,* 2007, vol. 164, pp. 31–47.

Wu, C.M., Zhang, J., and Ren, L.D., Empirical garnet–biotite–plagioclase–quartz (GBPQ) geobarometry in medium - to high-grade metapelites, *J. Petrol.,* 2004, vol. 45, no. 9, pp. 1907–1921.

Xiao, W., Windley, B.F., Badarch, G., et al., Paleozoic accretionary and convergent tectonics of the southern Altaids: implications for the growth of Central Asia, *J. Geol. Soc. London,* 2004, vol. 161, pp. 339–342.

Zeh, A., Millar, I.L., and Horstwood, M.S.A., Polymetamorphism in the NE Shackleton Range, Antarctica: constraints from petrology and U–Pb, Sm–Nd, Rb–Sr TIMS and in-situ U-Pb LA-PIMMS dating, *J. Petrol.,* 2004, vol. 45, pp. 949–973.

Translated by E. Kurdyukov